國 立 交 通 大 學

應用化學系碩士班

碩 士 論 文

利用交叉分子束方法形成 C_6D_6O, C_6H_6S 與 C_6D_6S 加合物

以及基態硫原子與苯反應的量子化學計算

Formation of Hot Adducts of C_6D_6O, C_6H_6S and C_6D_6S

in Crossed Molecular Beam Experiments and

Theoretical Calculations on the $S(^3P) + C_6H_6$ Reaction

研 究 生：李冠儀

指導教授：林志民　博士

中 華 民 國 一〇三 年 七 月

利用交叉分子束方法形成 C_6D_6O, C_6H_6S 與 C_6D_6S 加合物以及基態硫原子與苯反應的量子化學計算

Formation of Hot Adducts of C_6D_6O, C_6H_6S and C_6D_6S in Crossed Molecular Beam Experiments and Theoretical Calculations on the $S(^3P) + C_6H_6$ Reaction

研 究 生：李冠儀　　Student：Kuan-Yi Li

指導教授：林志民 博士　　Advisor：Dr. Jim Jr-Min Lin

國 立 交 通 大 學

應 用 化 學 系

碩 士 論 文

A Thesis Submitted to M. S. Program, Department of Applied Chemistry

College of Science

National Chiao Tung University

in partial Fulfillment of the Requirements

for the Degree of Master in Applied Chemistry

July 2014

Hsinchu, Taiwan, Republic of China

中華民國 103 年 7 月

摘要

本實驗中，我們利用交叉分子束生成氧原子(或硫原子)與苯(或氘代苯)的加合物，並對基態硫原子與苯的反應進行量子化學計算。

在交叉分子束實驗中，氧原子(或硫原子)以適當氣體經高壓放電產生，其中基態的氧原子及硫原子為主要產物。氧原子束(或硫原子束)與苯(或氘代苯)分子束交會後，反應的產物會在距離分子束碰撞點 10 公分處被同步輻射的真空紫外光游離，並由質譜分析偵測。

本實驗觀測了與加合物相關的母體離子及碎片離子，實驗數據顯示這些離子皆在相同的飛行時間抵達偵測器，其角度分布亦相互吻合，藉此我們推測這些離子可能來自同一中性產物。而在質心角度附近觀測到母體離子及碎片離子的訊號則顯示中性產物的速度向量在質心方向，且游離前中性產物並沒有分解而造成速度變化。根據交叉分子束實驗結果，我們判定觀測到的母體及碎片離子來自於長生命期的 C_6D_6O、C_6H_6S 及 C_6D_6S 加合物。此外，光游離效率圖更顯示硫原子與氘代苯反應產生的 C_6D_6S 加合物擁有較多的游離碎片與低游離能，其內能相較穩定的 Thiophenol 高了許多。然而，即使加合物的高內能使其熱力學上不穩定，我們發現這些加合物仍擁有超過百微秒的長生命期。

為了瞭解分子束實驗中 C_6D_6S 加合物可能的反應異構物及生成途徑，我們進一步進行基態硫原子與苯反應的量子化學計算。反應過渡態與中間態的幾何結構以及反應路徑(intrinsic reaction paths, IRC)首先以密度泛函方法 B3LYP/6-311G(d,p)計算，之後過渡態與中間態再以較高基組 aug-cc-pVTZ 做幾何結構優化。由計算結果我們推測反應可能進行的途徑如下：反應物原先在三重態位能面，經由 intersystem crossing 後(可能發生在類似 C_6H_6S diradical 的幾何結構)，在單重態位能面生成產物。單重態的 benzene sulfide 和 thiophenol 可能為 intersystem crossing 後首先生成的中間態，之後可能再形成其他的異構物。相較其他中間態，單重態的 thiophenol 擁有最低的位能，因此也較為穩定。此外，我們更進一步用 time-dependent M06 方法計算 intersystem crossing 可能發生區域的基態與激發態能量，並針對與 intersystem crossing 相關的中間態及過渡態進行 M06/aug-cc-pVTZ 幾何結構優化。

Abstract

In this work, we studied the formation of long-lived hot adducts in the O+C_6D_6, S+C_6H_6 and S+C_6D_6 reactions with crossed molecular beam method. Theoretical calculations related to the C_6H_6S adduct formation are also performed.

In the crossed molecular beam experiments, O (or S) atoms were generated with discharge and ground state O(^{3}P) and S(^{3}P) atoms were found to be predominant in these two atomic beams. After O (or S) atomic beam intercepted with C_6H_6 (or C_6D_6) beam, the products were photo-ionized by vacuum UV light from synchrotron radiation 10 cm away from the crossing point; the photo-ions were then mass-filtered and detected. For the studied reactions, the detected parent and daughter ions arrived at the detector almost at the same time and exhibited the same angular distribution, indicating they all correspond to the same neutral species.

Based on our experimental results, long-lived hot adducts of C_6D_6O, C_6H_6S and C_6D_6S are formed in the crossed beam condition. These products are detected at the angle of the center of mass, indicating zero recoil velocity. Photoionzation efficiency (PIE) curves of the C_6D_6S adduct and thiophenol sample were measured. In the PIE curves, lower ionization energy and more fragmentation are observed for the C_6D_6S adduct, consistent with the fact that this adduct has higher internal energy than the thiolphenol sample. Although the observed adducts have high internal energy and are thermodynamically unstable, their lifetimes may exceed the experimental time of flight which is in the order of hundreds of microseconds.

To determine the possible isomers for the C_6H_6S adduct and their formation pathways, we conducted theoretical calculation on the S(^{3}P) + C_6H_6 reaction. Geometry optimization of stationary points and intrinsic reaction paths (IRC) are carried out at B3LYP/6-311G(d,p) level of theory. These stationary points are then optimized again at B3LYP/aug-cc-pVTZ level. From the present data, we propose the most possible reaction paths are as follows. Reactants are originally on the triplet potential energy surface. Through intersystem crossing (possibly near the C_6H_6S diradical geometry), most isomers are then deposited on the singlet potential energy surface. Singlet benzene sulfide and thiophenol are supposed to be the first-formed intermediates, which may undergo further isomerizations. For all possible isomers, singlet thiophenol is found to be the most stable one. Furthermore, energies of ground and excited states near the intersystem crossing region are calculated by time-dependent density functional method, TD-M06 method. And for some stationary points which might concern singlet-triplet intersystem crossing are optimized by M06/aug-cc-pVTZ for better accuracy.

誌謝

這篇論文的完成要感謝好多人。首先要謝謝林志民老師這兩年來用心的教導，讓科學不只是儀器與數據，透過自己動手操作與組裝實驗設備，科學不再遙不可及。還有謝謝老師在我的實驗遇到瓶頸時，給了我很多中肯的建議。另外，謝謝老師讓大家有機會每周練習簡報，無論是簡報技巧或是論文的圖表呈現都讓我受益匪淺。謝謝高橋開人老師在我理論計算遇到困難時，很有耐心地為我解惑，並給了我不少建議，讓理論計算部分能順利進行。謝謝李遠哲院長每周二的會面時間，讓我從中學到了很多，並給了我們到同步輻射做實驗的構想。謝謝倪其焜老師、曾建銘老師特地抽空指導我的口試，給了我很多論文上的建議。

另外我要特別感謝金兵學長非常用心地教導我實驗技巧與理論計算，並提供很多學習資料讓我參考。謝謝同步輻射中心的李世煌老師慷慨出借電極設備，黃文建學長協助我架設儀器，孫翊倫學長教導我理論計算。還有謝謝原分所的李敬焘先生領我入理論計算之門。

感謝我的爸爸媽媽在我一邊做實驗一邊準備交換學生時給了我很多支持與鼓勵。謝謝我的實驗室夥伴家彬和我一起熬夜做實驗，謝謝啟佑與潘世傑學長在我剛進實驗室時給我很多的照顧。另外，感謝我的好友沂蓁，即使遠在美國也時常為我加油打氣，還有謝謝耘禎、靖文、諭嫻讓我在台大校園也有家的感覺。最後我想感謝交大、原分所與同步輻射中心所有人的指導與協助，讓我能夠順利完成實驗！

Contents

Table List

Figure Captions

Chapter I Introduction

The reaction between benzene and O atom is an important issue in both combustion chemistry and atmospheric chemistry because benzene is the crucial chemical of forming polycyclic aromatic hydrocarbons (PAHs) in the air. A large amount of research on kinetics of benzene and ground state $O(^3P)$ atom has been reported previously. Several reaction channels were investigated in experimental and theoretical works, including spin allowed and spin forbidden paths[1]. The followings are the products of $O(^3P) + C_6H_6$ reaction[2]:

$$C_6H_6 + O(^3P) \rightarrow C_6H_5O\cdot + H\cdot \quad (1)$$

$$\rightarrow C_6H_5OH \quad (2)$$

$$\rightarrow \text{isomers of } C_6H_5OH \quad (3)$$

$$\rightarrow C_5H_6 + CO \quad (4)$$

O-addition onto carbon atom is thought to be the first step of these reaction paths. Triplet diradical C_6H_6O is formed through O-addition and this intermediate will further proceed to the major products listed above[1-3]. Phenoxy plus H radicals (1) are formed through spin allowed H-detachment path. They were first detected by Lee and coworkers[3] in crossed molecular beam experiments. And this channel was further reinvestigated by Fontijn and coworkers [4] in multi-collision conditions with flow tube.

Triplet diradical also undergoes intersystem crossing to form singlet products. Singlet phenol (2) is another major product of $O(^3P) + C_6H_6$ reaction. It is found to have very long lifetime in crossed beam experiments[3]. Nguyen et al.[1] have proposed the reaction paths on the ground state singlet potential energy surface with high-level CBS-QB3 method. Figure1-1 shows the reaction paths start from singlet phenol. In this figure, singlet phenol is calculated to have minimum potential energy. Because the total energy is high, it can further isomerize to other singlet isomers [1].

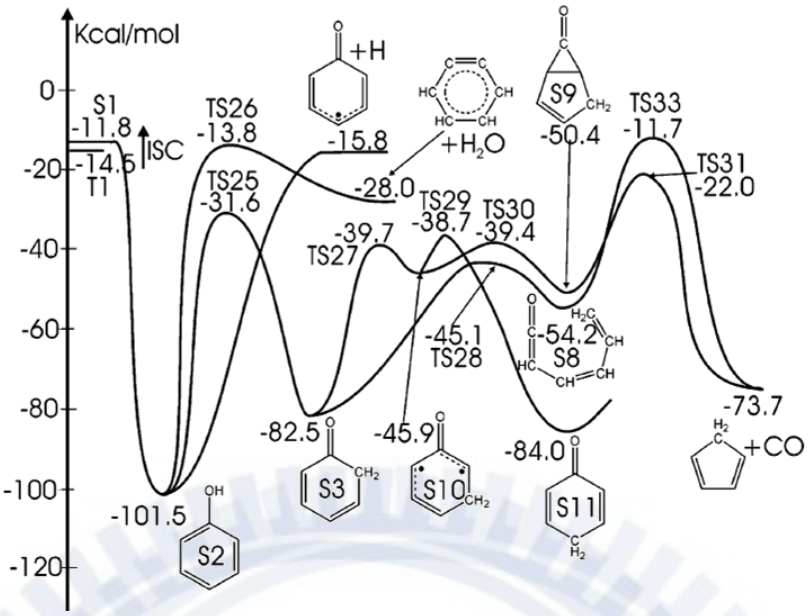

Figure1-1 Part of reaction paths on singlet potential energy surface calculated at CBS-QB3 level by Nguyen et al.[1] The energy reference here is the total energy of $O(^3P) + C_6H_6$.

Benzene oxide and cyclohexadienone are other isomers of phenol detected in the experiments. Parker and Davis[5] have conducted photolysis experiments on O_3 and benzene in a solid Ar matrix, and found out these two isomers are the products in the reaction between $O(^3P)$ atom and benzene. CO elimination (4) was regarded as a minor pathway by Lee and coworkers[3]. Further results from theoretical calculations indicated C_5H_6 + CO formation is significant only when temperature is higher than 700K [2].

In this work, we conducted crossed beam experiments on $O(^3P) + C_6D_6$ reaction with much better resolution than Lee's work. We were quite interested in the formation of the long-lived C_6D_6O adduct, and therefore mainly focused on its parent mass (m/z=100 signal) in this reaction.

S atom shows similar characteristics to O atom, and it also plays an important role in combustion of S-containing fuel and coals. However, compared to well-established research on O atom and hydrocarbons, there were only limited reports on the kinetics of the reaction between S atom and hydrocarbons [6-12]. Matsui and coworkers[6] have carried out the shock-tube experiments on the reaction between $S(^3P)$ atom and several

saturated hydrocarbons (such as CH_4, n-C_4H_{10} and etc.). They have measured the rate constants of these reactions at temperature above 830K. In recent years, Casavecchia and coworkers[7-9] have investigates the reaction between S(^{1}D) atom and unsaturated hydrocarbons, such as C_2H_4 and C_2H_2. Both the crossed beam experiments and theoretical work have been done for the dynamics of these reactions. However, the reaction between S(^{3}P) atom and aromatic ring still remains unexplored.

In lack of kinetic data, we presented the first report on the crossed beam experiment on the reaction between ground state S(^{3}P) atom and benzene. In this work, we carry out the experiments on both S + C_6H_6 and S+ C_6D_6 reaction; we especially focused on formation of adducts, as followings show.

$$C_6H_6 + S(^3P) \rightarrow C_6H_6S$$

$$C_6D_6 + S(^3P) \rightarrow C_6D_6S$$

To our knowledge, most of the articles related to theoretical calculations of C_6H_6S are for decomposition of thiophenol (C_6H_5SH). Lim et al.[10,11] mainly focused on photoinduced H-detachment path of thiophenol at 243 nm and other wavelengths. Al-Muhtaseb[12] et al. proposed the geometries of some possible intermediates and the energy diagram for pyrolysis of thiophenol. To better understand the reaction dynamics of S(^{3}P) + C_6H_6 and the relative energies of possible C_6H_6S adduct conformers, we made a lot of efforts on the theoretical study of this system.

Chapter II Experimental Section

2.1 Crossed Molecular Beam Experiments

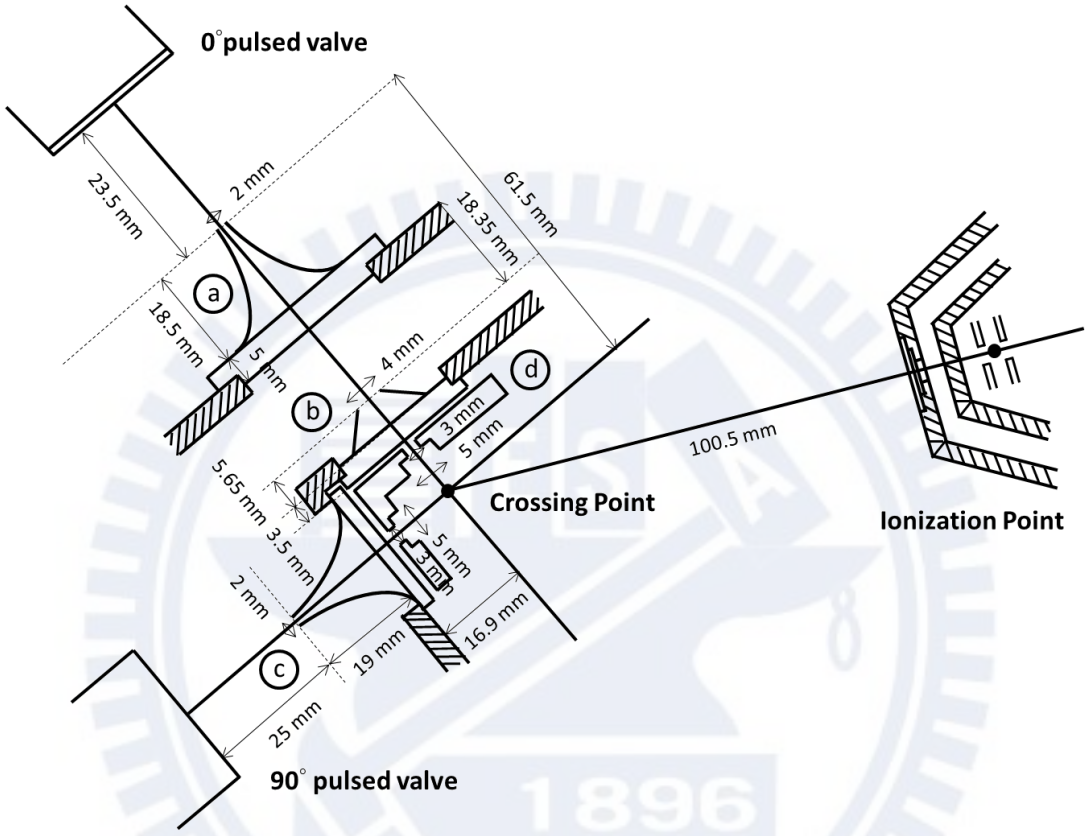

Figure 2-1 Schematics of the crossed molecular beam setup in this work. (a) first skimmer for 0° molecular beam (in SC-I) (b) second skimmer for 0° molecular beam (in SC-I) (c) skimmer for 90° molecular beam (in SC-II) (d) cold panel (for diminishing background, in main chamber) Note that not all components here are to scale.

Instrument for the crossed beam experiments can be generally divided into three parts: source chamber, main chamber and detection chamber. The details will be discussed in section 2.1.4. Figure 2-1 shows the arrangement of the major components for crossed beam experiments in this work. O atom and S atom beam were generated at 0° pulsed valve (Even-Lavie type) with discharge device in Source Chamber-I (SC-I in Figure 2-5). C_6H_6, C_6D_6 and C_6H_5SH molecular beam were ejected from 90° pulsed valve

(Even-Lavie type) with heating device in Source Chamber-II (SC-II). The crossing point of the two beams is in the main chamber, and then the initial products will be ionized by synchrotron radiation at ionization point in the detection chamber.

2.1.1 Molecular Beam Preparation

We followed the method done by Lee et al.[13] to generate O atom beam. In their experiments, they generated O atom with two kinds of discharge medium, 3% O_2 + 12.5% Ar (in He) and 20% O_2 (in He). In our experiment we only exploited 20% O_2 (in He) as discharge medium because this mixture was reported to have good performance in producing ground state O (^3P) atom[13].

Photolysis of S-containing compounds is a common way to generate S(^3P) atoms. Lee and coworkers obtained S(^3P) by photolysis of OCS at 248nm[14]. However, the absorption cross section of OCS is in the order of 2.338×10^{-20} cm^2 at 295K[15], which might be too small to generate enough amounts of S atoms for single-collision experiments. We thought high-voltage discharge of S-containing molecules might be more suitable to generate S atom beam for crossed beam experiments. Therefore, 3% CS_2 vapor (in Ne) was chosen as the discharge media in our case.

To initiate discharge and keep it stable, the backing pressure of the discharge media needs to be 100 psia or higher. Because CS_2 is in liquid phase at room temperature, it needs to evaporate first before mixed with Ne in the cylinder. Consequently, even if it is better to increase CS_2 density in discharge media to create more S atoms, CS_2 vapor was premixed with the Ne buffer gas to make a 3% mixture. It was the results of a balance between vapor pressure of CS_2 (6.85 psia at 298K) and 100 psia backing pressure requirement.

Without demand of discharge at 90° pulsed valve, backing pressure and even the density of molecular beam is much easy to control. Here we use a bubbler to generate C_6H_6, C_6D_6 and C_6H_5SH molecular beam. With bubbler, we can change the backing pressure by regulating the blowing pressure of buffer gas (Ne is used here). And the density of C_6H_6 (or other species) can be altered by changing the temperature of C_6H_6 liquid (change the vapor pressure of it). In our experiments, the temperature for C_6H_6, C_6D_6 and C_6H_5SH liquid were all 298K. The backing pressure of C_6H_6 and C_6D_6 beams were around 55 psia, and that of C_6H_5SH beam was 23.8 psia. Besides, to avoid clustering of C_6H_6, C_6D_6 and C_6H_5SH molecules during ejection from pulsed valve (supercooling process), we used heating apparatus to increase the temperature of the nozzle to 398K.

Ne was used as buffer gas here. The beam speed is slower and suitable for detector responding time when we choose Ne than He. And compared to Ar, tendency to form clusters is also less for Ne. Therefore, Ne is the most suitable buffer gas in our case.

2.1.2 Pulsed-High Voltage Discharge Device

In this work, we used pulsed-high voltage discharge device designed by Huang et al. [16] to generate O atom beam and S atom beam. Figure 2-2 shows details of discharge device on 0° pulsed valve.

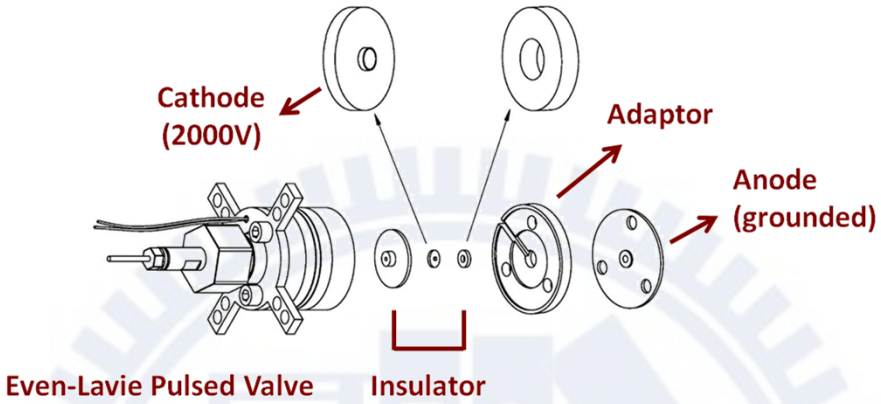

Figure 2-2 Discharge Device (Components contour by Huang et al.[16])

The discharge media are first ejected by Even-Lavie pulsed valve, and then discharged by stainless steel electrodes (Cathode and Anode in the figure). The insulators are made of ceramic, which can avoid the two electrodes and Even-Lavie valve from contacting with each other. The Teflon adaptor is used to arrange the small insulators and cathode in the right positions. The 3 holes (in triangle array) in the adaptor, anode, and Even-Lavie valve are for the screws to fix all the components together.

The repetition rate for both 0° pulsed valve, 90° pulsed valve and discharge were synchronized by a delay generator DG-535 pulse generator and were set to be 200Hz (or 100Hz for optimizing signals). Pulse widths of two molecular beams were both 20 μs, and discharge time width was set to be 10 μs. Time delay between the two molecular beam pulses and discharge starting time were also controlled by DG-535.

Figure 2-3 shows TOF (time of flight) spectra of S atom from discharging 3% CS_2 (in Ne) with instrument describing here. Different lines are TOF spectra at different detection angles. After integrating signals at different detection angles, we can plot the

angular distribution of S atom, as Figure 2-4 shows. The distribution was fitting by Gauss curve; we can find out the angle with the largest intensity is at -0.2°, and FWHM (Full width at half maximum) of the angular distribution is around 1.4°.

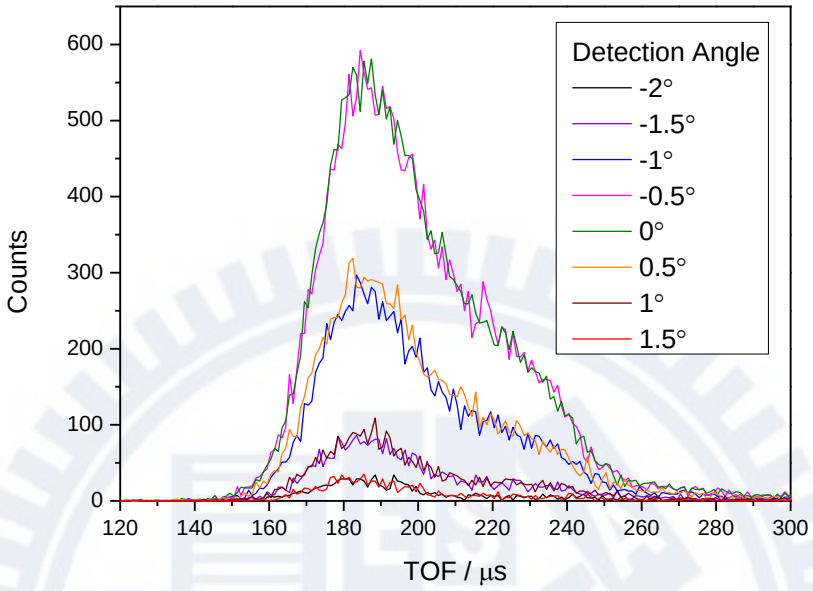

Figure 2-3 TOF spectra of the S atomic beam at different detection angles. The time zero was set at the beginning of the discharge interval, and the ion flight time is removed here. Before the S atoms arrive at the crossing point, they fly through 85 mm distance and it takes 71 μs for the flight.

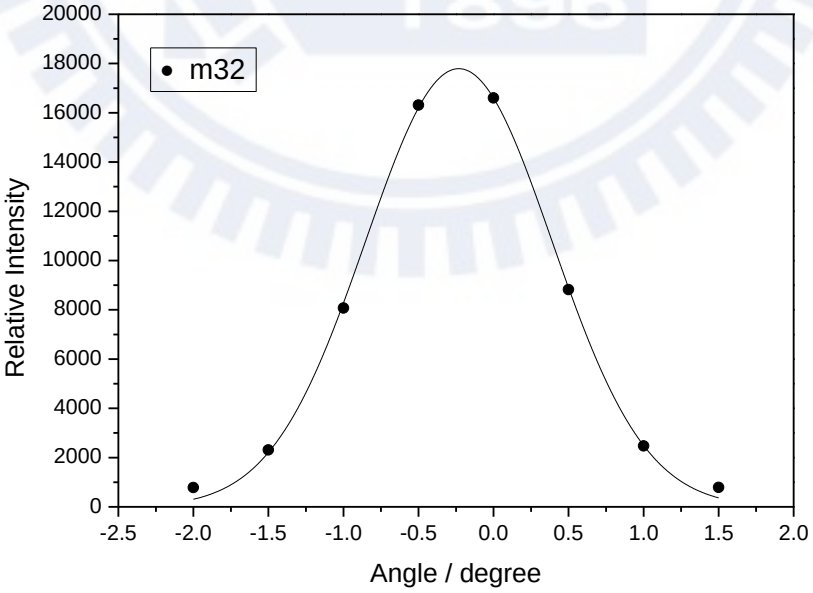

Figure 2-4 Angular distribution of the S atomic beam from discharging the CS_2 gas mixture. The largest signal appears at -0.2°, and FWHM of the angular distribution is 1.4°. The photon energy for ionization is 10.25 eV.

2.1.3 Ionization by Synchrotron Radiation Light

Photoionization is regard as soft ionization method because the energy used for photoionization is much lower than other ionization method. In this work, beam line 21A (BL21A) in National Synchrotron Radiation Research Center (NSRRC) was used as the ionization light source.

With higher ionization energy, intensity of signal gets stronger and signal-to-noise ratio (S/N) also increases. However, higher photon energy might cause dissociative ionization of neutral molecules. Therefore, choosing a suitable energy range is crucial.

In the gas cell we arranged Ar as gas filter for O atom + C_6D_6 experiments, and Kr for S atom + C_6H_6 (also C_6D_6) experiments. Light source with energy higher than 15.7 eV will be absorbed by Ar and will not get into the ionization region of crossed beam instrument. And Kr blocks radiation with energy higher than 14.1 eV. Besides, energy of radiation can be adjusted during the experiment by changing the gap between two magnets arrays of the undulator. Energy range for photoionization efficiency curve is selected to be 7.02-11.71 eV in this work, and the energy of radiation for each time of flight spectra is chosen around ionization energy of each species.

2.1.4 Instrument Detail

Figure 2-5 shows the vertical cross section of the instrument in this work. As mentioned in the previous section, instrument for crossed beam experiments can be generally divided into three parts: source chamber, main chamber and detection chamber. Source chambers, main chamber and detection chamber are kept at 8.2×10^{-9}, 10^{-8} and 2.8×10^{-11} torr respectively without gas loading. During O atom + C_6D_6 and S atom + C_6H_6/C_6D_6 experiments, 0° source chamber was kept at $2\text{-}5\times10^{-5}$ torr, and 90° source chamber was kept at $5\text{-}7\times10^{-6}$ torr. For C_6H_5SH experiments, 90° source chamber is kept at lower pressure, 8.9×10^{-7} torr.

0° and 90° pulsed valves are set in Source Chamber-I and II (SC-I and SC-II) respectively. The two source chambers are fixed at 90° with each other, and they can be rotated together from -20° to 110°. Therefore, products formed at crossing point can be detected from different lab angles by the fixed detector. 0° and 90° skimmers are used to confine angular dispersion of molecular beams. Two skimmers are used for 0° beam, and one is for 90° beam.

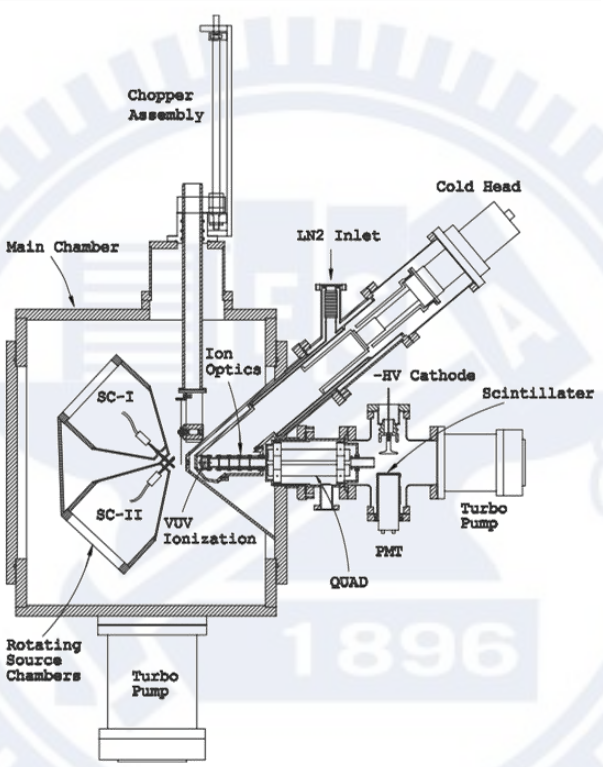

Figure 2-5 Scheme of the crossed molecular beam instrument[13].

Main chamber is where the reaction takes place. At the entrance into main chamber, there is an L-shaped cold panel with two 3mm orifices (each for one beam), as Figure 2-1 (d) shows. Cold panel is used to trap rebounded molecules which are not in the direction of molecular beam. Cooling by He refrigerator to nearly 10K, the copper-made cold panel substantially diminishes background, and thus increases S/N ratio.

The distance between crossing point and ionization point is 100.5 mm. At the entrance into ionization region, another liquid-nitrogen trap is used to decrease the background of

detection region. After ionization, ions with different masses are separated by quadrupole mass filter, and then detected by Daly-type ion counter.

2.2 Theoretical Calculation

We like to learn more about the conformations of products detected in the crossed molecular experiments; however, due to the limitation of mass spectrometry, we only know the masses of the products but little about their structures. Therefore, theoretical calculation is needed for understanding the details of the reaction dynamics.

There are a lot of theoretical articles discussing the reaction path between O atom and C_6H_6, but there is no theoretical report about S atom and C_6H_6 reaction. In this work, we put emphasis on the reaction of S atom and C_6H_6. Besides, we found S atoms generated from discharging CS_2 are mainly in the ground state, and hence we focused on the reaction between S (^3P) and C_6H_6 in the computational section.

All the calculations are done by Gaussian 09 package[17]. The geometries and vibrational frequencies for the ground-state stationary points which might be related to the reaction are first obtained by B3LYP/6-311G(d,p)[18,19]. Intrinsic reaction paths (IRC) are then found by B3LYP/6-311G(d,p). To get better geometries, we optimized both the intermediates and transition states we have found with higher basis set B3LYP/aug-cc-pVTZ[18,20]. Besides, for some stationary points which might concern singlet-triplet intersystem crossing are optimized by M06/aug-cc-pVTZ [20,21]. M06 is the hybrid functional developed by Zhao and Truhlar[21], and it is suggested to have better performance on main group molecules than B3LYP. We also use time-dependent M06/6-311G(d,p) method to find the relative energies of the ground state and excited states near the crossing point of singlet and triplet potential energy surfaces.

Chapter III Result and Discussion

3.1 Results from Crossed Molecular Beam Experiments

3.1.1 O atom + C_6D_6 Reaction

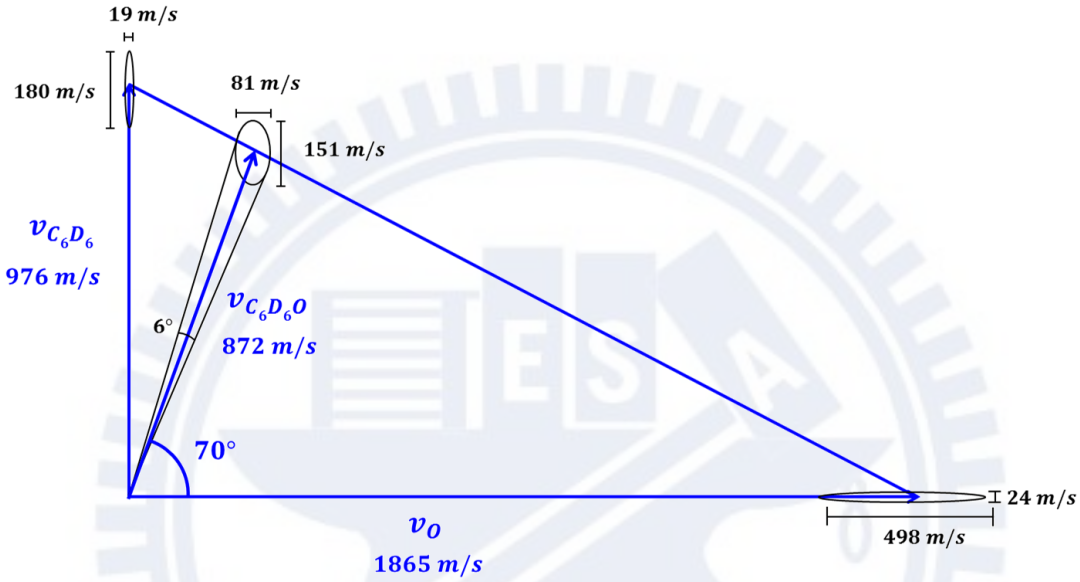

Figure 3-1 Newton diagram for the reaction between O atom and C_6D_6. The angle 70˚is from the Gaussian fitting of the angular distribution data of $C_6D_6O^+$ (m100) signal. The error bars of the C_6D_6 and O atom velocities are calculated by matching the time of flight (TOF) spectra of C_6D_6 and O atom.

In this section, we will discuss the data from crossed beam experiment of O atom + C_6D_6. Figure 3-1 shows the newton diagram of the reaction between O atom and C_6D_6. C_6D_6O adduct is found at the angle of the center-of-mass, lab angle 70˚.

3.1.1-1 O atom beam produced from discharging O_2

Angular distribution of O atom generated at 0˚ pulsed valve is plotted as Figure 3-2. The distribution is fitting by Gauss curve. The largest signal appears at -0.2˚, and FWHM of the angular distribution is around 1.2˚.

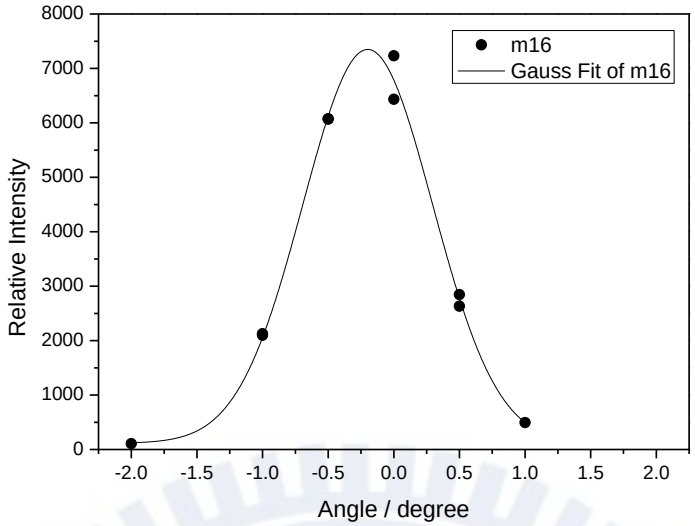

Figure 3-2 Angular distribution of the O atomic beam from discharging O_2. The largest signal appears at -0.2°, and FWHM of the angular distribution is 1.2°.

Figure 3-3 shows photoionization efficiency (PIE) curve of O atom beam from discharging 20% O_2 (in He) in this work. The ionization thresholds for $O(^3P)$ and $O(^1D)$ are at 13.62 and 11.65 eV, which correspond to ionization processes $O(^3P) \rightarrow O^+(^4S^0) + e^-$ and $O(^1D) \rightarrow O^+(^4S^0) + e^-$, respectively[13,22]. Between 11.65 and 13.62 eV, only $O(^1D)$ atoms are ionized; both $O(^3P)$ and $O(^1D)$ atoms cam be ionized when photon energy is larger than 13.62 eV.

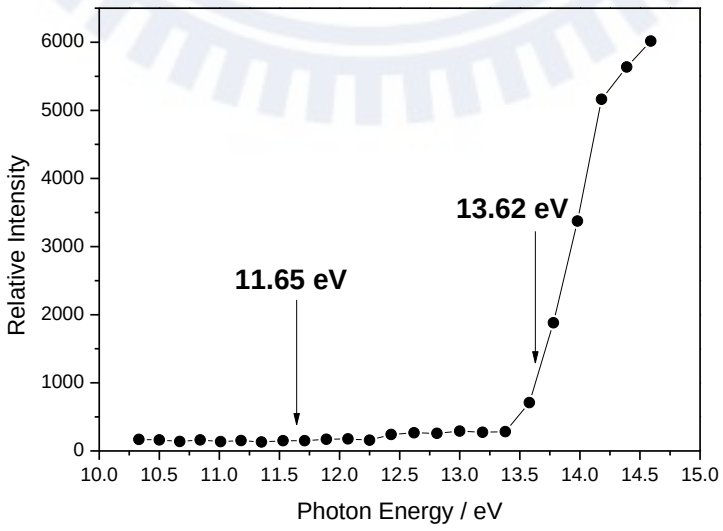

Figure 3-3 Photoionization efficiency curve of the O atom (m16 signal) reactant in this work.

Lee et al.[23] has recorded PIE curves of $O(^1D)$ and $O(^3P)$ atoms. In their PIE curves, the photoionization cross section for pure $O(^3P)$ source at 13.98 eV to that for pure $O(^1D)$ source at 12.62 eV is 0.4 ($\frac{\sigma_{ion}^{O(^3P)}(13.98\ eV)}{\sigma_{ion}^{O(^1D)}(12.62\ eV)} = 0.4$). We can therefore estimate the $O(^1D)$ population in our experiment to be 1.51% of all O atoms.

Most abundant O atoms are in the ground state $O(^3P)$. The result is the same as that from Lee's work[13]. It is because the rate coefficient of reaction $O(^1D) + O_2 \rightarrow O(^3P) + O_2$ is rather high ($(4.1 \pm 0.5) \times 10^{-11}$ cm^3 $molecule^{-1}$ S^{-1} at 298K[24]), most $O(^1D)$ atoms are depleted to ground state by O_2. Therefore $O(^3P)$ atoms are the dominant species in this work.

3.1.1-2 Photoionization Efficiency Curve of C_6D_6

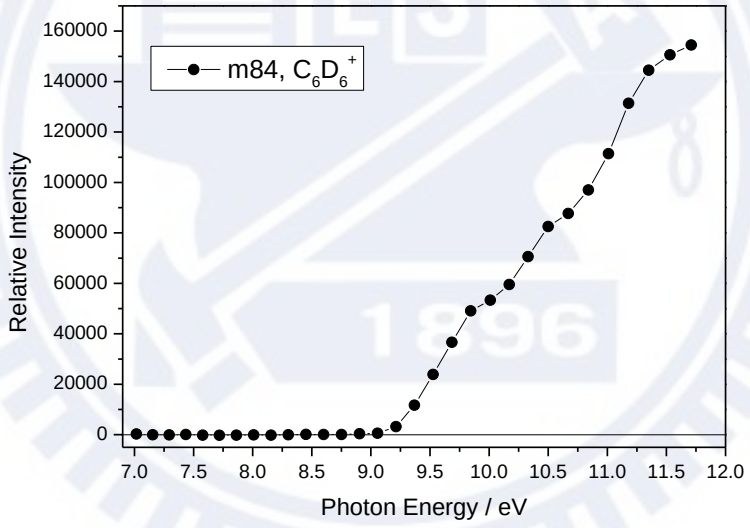

Figure 3-4 Photoionization efficiency curve of C_6D_6.

Figure 3-4 shows the PIE curve of $C_6D_6^+$ from C_6D_6 molecular beam in this work. The ionization energy of C_6D_6 in this figure is about 9.24 eV, which coincides well with the ionization energy of C_6D_6 measured by Person[25]. Person has also recorded the photoionization efficiencies (η) of C_6H_6. We didn't measure the PIE curve of the C_6H_6 beam; however from Person's result[25], the ionization energy of C_6H_6 is known to be close to that of C_6D_6, 9.24 eV.

3.1.1-3 O atom + C_6D_6 Reaction

We have detected the parent ions of the C_6D_6O adducts, which correspond to the m100 signal in Figure 3-5. The $C_6D_6O^+$ ions are detected in the direction of center-of-mass, indicating there is no recoil velocity for the adducts. Although photoionization is called "soft ionization" method (compared to average 70 eV for electron impact ionization method), the photon energy might cause dissociative ionization of C_6D_6O adducts. Therefore, beside parent ion $C_6D_6O^+$ (m100 signal), we also detected signals from its possible daughter ions: $C_6D_5O^+$ (m98 signal), $C_5D_6^+$ (m72 signal) and $C_5D_5^+$ (m70 signal).

From Figure 3-5, we can find out the signals of $C_6D_6O^+$, $C_6D_5O^+$, $C_5D_6^+$ and $C_5D_5^+$ all arrive at the detector at the same time, which implies there are only C_6D_6O adducts formed at the collision point and all the other fragments are further generated from C_6D_6O adducts during ionization process. Before being ionized, the long-lived C_6D_6O adducts do not decompose to other fragments during 100.5 mm field-free flight. Their lifetimes likely exceed the experimental time of flight which is 115 μs.

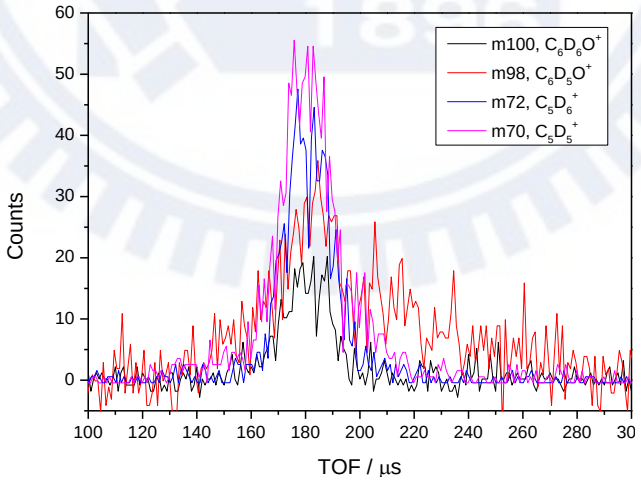

Figure 3-5 TOF spectra of m100, m98, m72 and m70 signals detected at 70°. (The curves are from integration of 200k, 800k, 30k and 30k pulses for m100, m98, m72 and m70 signals, respectively.) The ionizing photon energy is 11.35 eV. The time zero was set at the beginning of the discharge interval, and the ion flight time is removed here. Before the O atomic beam intercepts with the C_6D_6 beam, O atoms fly through 85 mm distance (from the discharge position to at the crossing point), and it takes 46 μs for the flight.

From the previous section, the ionization energy of C_6D_6 is close to 9.24 eV. In some cases, the photon energy we chose to ionize products might exceed 9.24 eV and produce daughter ions of the same masses as those of C_6D_6O adducts, for example $C_5D_6^+$and $C_5D_5^+$. It seems the signal from C_6D_6 might confuse us. However, the scattering angles for C_6D_6 and C_6D_6O are different. The daughter ions of C_6D_6 will be mostly detected at lab angle 90°. And according to momentum conservation, the signal from C_6D_6O adducts appears at lab angle 70°($\theta=\tan^{-1}\frac{168\times v_{C_6D_6}}{16\times v_O}$). Different scattering angles make it possible to distinguish between these two species. Besides, we don't have to worry about the contributions from the daughter ions of $(C_6D_6)_2O$ (if $(C_6D_6)_2$ still forms after heating C_6D_6), the signal of $(C_6D_6)_2O$ might appear at lab angle 80°.

Figure 3-6, Figure 3-7 (a) and (b) are the PIE curves of $C_6D_6O^+$, $C_5D_6^+$ and $C_5D_5^+$ detected at 70°, respectively. The ionization energy of C_6D_6O product in this work is much lower than the ionization energy of phenol, 8.5 eV. This indicates the C_6D_6O adduct has higher internal energy than phenol, and thus less energy is required for ionization. The ionization thresholds for $C_5D_6^+$ and $C_5D_5^+$ are also higher than that for $C_6D_6O^+$. It is quite reasonable because extra energy is needed for bond scissoring.

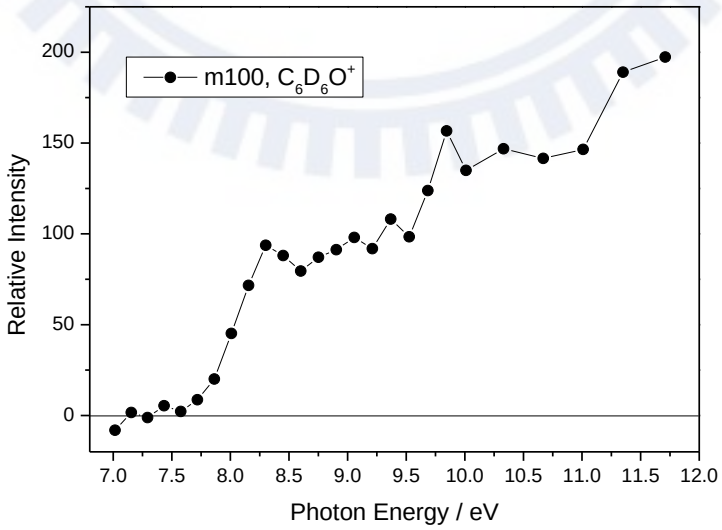

Figure 3-6 Photoionization efficiency curve of $C_6D_6O^+$ from the O + C_6D_6 reaction at 70°.

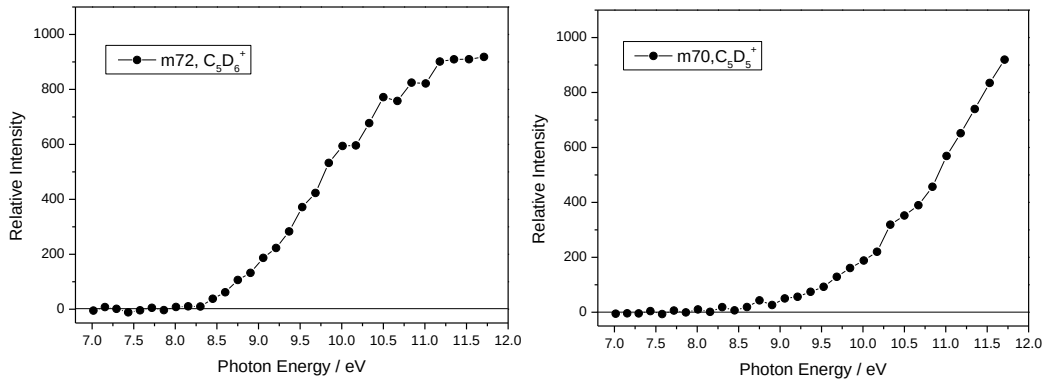

Figure 3-7 Photoionization efficiency curve of (a) $C_5D_6^+$ (m72 signal) (b) $C_5D_5^+$ (m70 signal) from the O + C_6D_6 reaction at 70°.

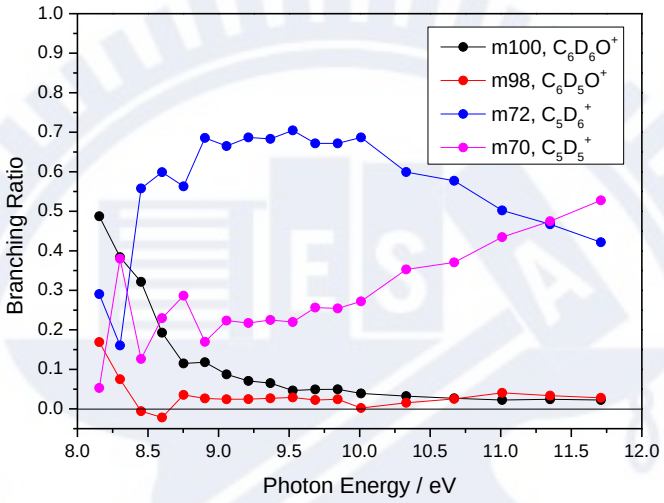

Figure 3-8 Branching Ratios of forming $C_6D_6O^+$ (m100), $C_6D_5O^+$ (m98), $C_5D_6^+$ (m72) and $C_5D_5^+$ (m70) ions in the O + C_6D_6 reaction at 70°. (Total are the summation of the intensities of these four products in the PIE curves.)

Figure 3-8 shows the branching ratios of forming $C_6D_6O^+$, $C_6D_5O^+$, $C_5D_6^+$ and $C_5D_5^+$ ions at different photon energies. At 8.1 eV, the most abundant ion is $C_6D_6O^+$. As photon energy increases, the ratios of the $C_6D_6O^+$ and $C_6D_5O^+$ ions decrease, and in the meanwhile the ratio of $C_5D_6^+$ ions increases. The signal of $C_5D_5^+$ ions also slightly rises (the sudden increase at 8.3 eV was thought to be fluctuations). The phenomena imply $C_5D_6^+$ and $C_5D_5^+$ might be generated from dissociative ionization of the C_6D_6O adducts, and $C_5D_6^+$ are the dominant species in this energy region. At 10 eV, the signal of $C_5D_6^+$ begins to decrease and the signal of $C_5D_5^+$ increases. This indicates more $C_5D_5^+$ ions are generated from dissociation of $C_5D_6^+$ ions as photon energy higher than 10 eV.

3.1.2 S atom + C_6H_6 and S atom + C_6D_6 Reaction

In section 3.1.2, we will first analyze the S atom generated by discharge. Then we will discuss the results from S atom + C_6H_6 and S atom + C_6D_6 experiments.

3.1.2-1 S atom beam produced from discharging CS_2

Lee and coworkers[26] have reported the photoionization spectra of S atom with synchrotron radiation light ranging from 9.36-11.10 eV (75 500-89 500 cm^{-1}). In their study, it shows there is no absorption band for ground state S(^{3}P) atom but only excited S(^{1}D) atom when photoionization energy smaller than 10.53 eV (84 892 cm^{-1}) .

Figure 3-9 shows the photon ionization efficiency curve of S atom beam from discharging CS_2 in this work. Based on Lee's result[26], the increase of intensity around 9.69 eV is mainly contributed by S(^{1}D) atom, and the peak around 10.84 eV results from the absorption of both S(^{1}D) and S(^{3}P) atoms.

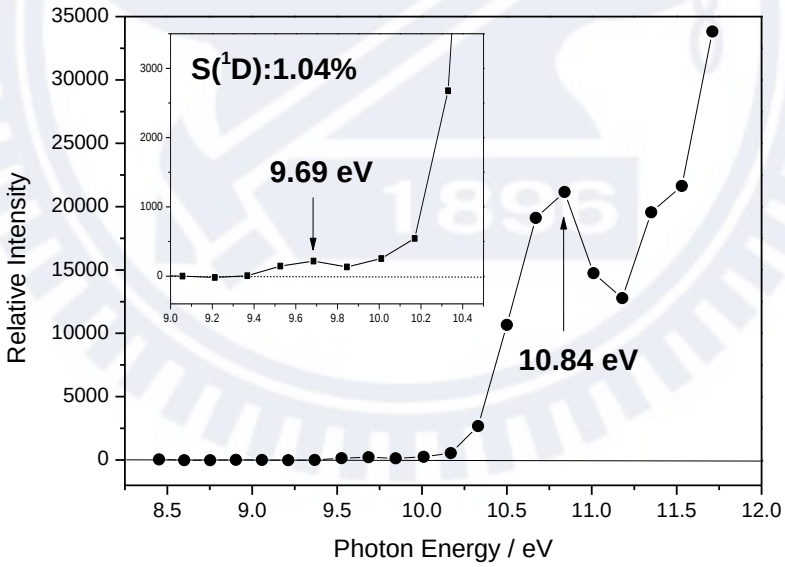

Figure 3-9 Photoionization efficiency curve of the S atomic beam.

To simplify the calculations on the ratios of S(^{3}P) and S(^{1}D) in S atom beam, we assumed the photoionization cross sections of S(^{3}P) at 9.69 eV and S(^{1}D) at 10.84 eV are the same. Therefore, the intensity at 9.69 eV refers to the amounts of S(^{1}D) atoms. And at 10.84 eV, the contributions from S(^{3}P) and S(^{1}D) atoms depend on their relative

amounts. Thus, we can calculate the relative amount of S(^{3}P) atom by simply subtracting the intensity at 9.69 eV from that at 10.84 eV. The ratio S(^{1}D) atoms is only 1.04% in our experiments.

3.1.2-2 Formation of the C_6H_6S adduct from S atom + C_6H_6 crossed beam reaction

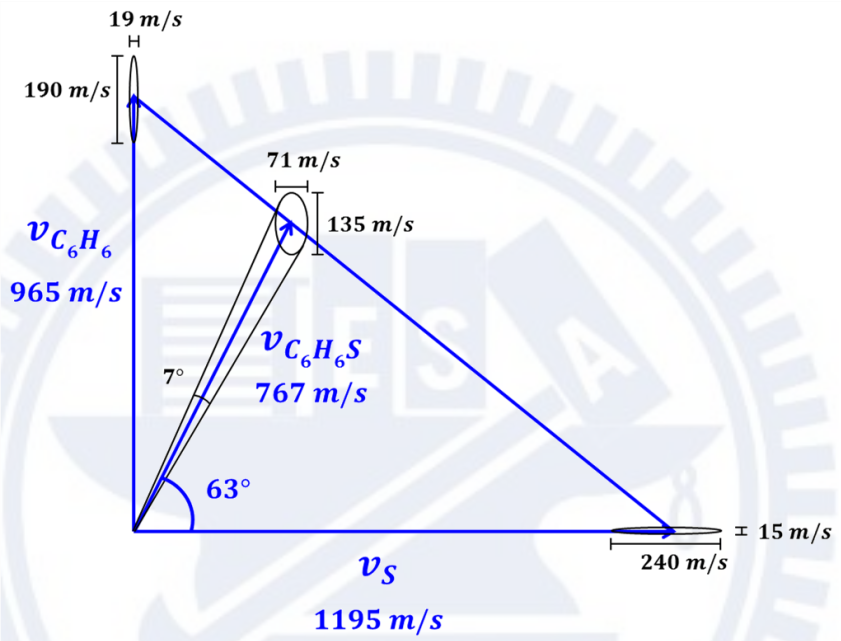

Figure 3-10 Newton diagram for the reaction between S atom and C_6H_6. The angle 63˚is from the Gaussian fitting of the angular distribution data of $C_6H_6S^+$ (m110 signal). The error bars of the C_6H_6 and S-atom velocities are calculated by matching the TOF spectra of C_6H_6 and S atom.

Figure 3-10 shows the newton diagram of forming C_6H_6S adduct in S + C_6H_6 reaction. The signal of $C_6H_6S^+$ (m110 signal) has been detected at the center-of-mass angle 63˚, which indicates there is no recoil velocity for the C_6H_6S adducts. As mentioned in section 3.1.1-3, we don't have to worry about the contributions from the daughter ions of $(C_6H_6)_2S$ either. The signal of $(C_6H_6)_2S$ might appear at lab angle 76˚. In this work, we mostly detected the parent ion and the possible daughter ions of C_6H_6S adduct at 63˚. However, due to discharging conditions of S atom beam and stability of C_6H_6 bubbler, in seldom cases the signals are detected at 64˚ for stronger signals.

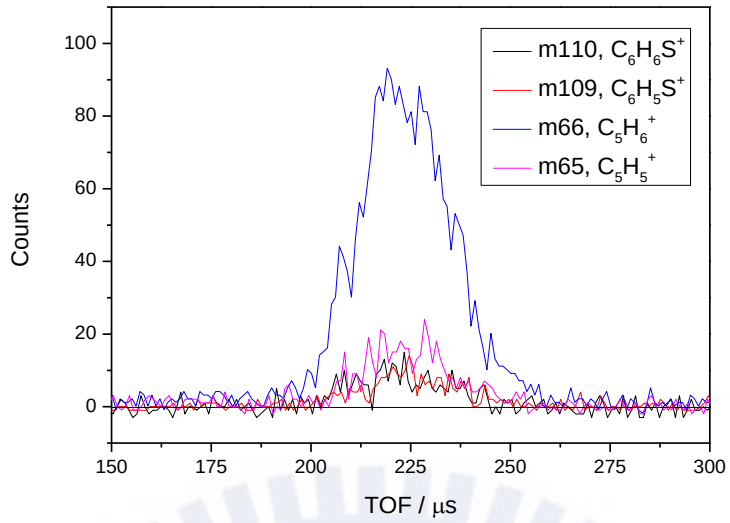

Figure 3-11 TOF spectra of m110, m109, m66 and m65 signals at 64°, which correspond to $C_6H_6S^+$, $C_6H_5S^+$, $C_5H_6^+$ and $C_5H_5^+$, respectively. (The curves are from integration of 150k, 50k, 100k and 100k pulses for m110, m109, m66 and m65 signals, respectively.) The ionizing photon energy is 11.71 eV. The time zero was set at the beginning of the discharge interval, and the ion flight time is removed here. Before the S atomic beam intercepts with the C_6H_6 beam, the S atoms fly through 85 mm distance (from the discharge position to the crossing point), and it takes 71 μs for the flight.

Figure 3-11 shows the TOF spectra of m110, m109, m66 and m65 products, which correspond to $C_6H_6S^+$, $C_6H_5S^+$, $C_5H_6^+$ and $C_5H_5^+$, respectively. The ion flight time and the background are removed in this figure. We can find out the arrival time of these four ions are almost the same. Figure 3-12 is the scaled TOF spectra from Figure 3-11. The TOF spectra of $C_6H_6S^+$, $C_6H_5S^+$, $C_5H_6^+$ and $C_5H_5^+$ are scaled to nearly the same height, and we can find out the distributions of these spectra look similar. Both Figure 3-11 and Figure 3-12 show that before ionized by synchrotron radiation, C_6H_6S adduct does not decompose to other small fragments. The $C_6H_6S^+$, $C_6H_5S^+$, $C_5H_6^+$ and $C_5H_5^+$ are parent ion and daughter ions of C_6H_6S adduct during ionization process. The lifetime of this long-lived adduct is estimated to exceed 130 μs.

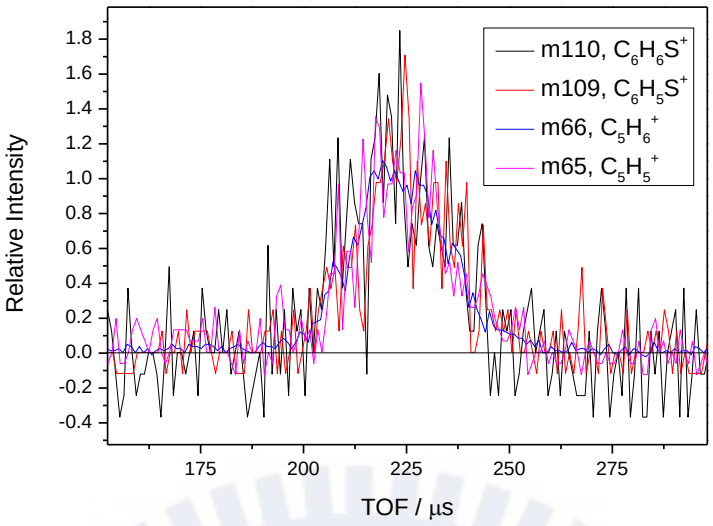

Figure 3-12 Scaled TOF spectra of $C_6H_6S^+$, $C_6H_5S^+$, $C_5H_6^+$ and $C_5H_5^+$ at 64°. The time zero was set at the beginning of the discharge interval, and the ion flight time is removed here. Before the S atomic beam intercepts with the C_6H_6 beam, the S atoms fly through 85 mm distance and it takes 71 μs for the flight.

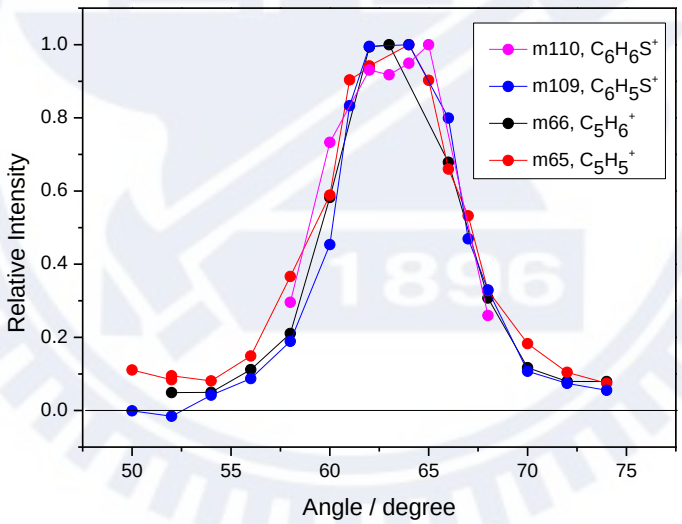

Figure 3-13 Angular distributions of $C_6H_6S^+$, $C_6H_5S^+$, $C_5H_6^+$ and $C_5H_5^+$.

The angular distributions of the $C_6H_6S^+$, $C_6H_5S^+$, $C_5H_6^+$ and $C_5H_5^+$ ions are also evidence for conclusions above. After the intensity of angular distributions are scaled to the same height, the width of these four distributions fit well with each other. It's clear that $C_6H_6S^+$, $C_6H_5S^+$, $C_5H_6^+$ and $C_5H_5^+$ are not decomposed from other products but only C_6H_6S adducts.

3.1.2-3 m110 signal ($C_6H_6S^+$) and 66 signal ($C_5H_6S^+$) for the C_6H_6S adduct

Figure 3-14 (a) and (b) show the TOF spectra and scaled TOF spectra of $C_6H_6S^+$ and $C_5H_6^+$ with longer integral time to increase signal-to-noise ratio (S/N ratio). Arrival time and the shape of peak are almost the same for these two products. Because $C_5H_6^+$ is the most abundant in all parent and daughter ions of C_6H_6S adduct, largest S/N ratio of m66 signal decreases the influence from background. Therefore, in the following part, we measured the m66 signal to represent the behavior of C_6H_6S adduct.

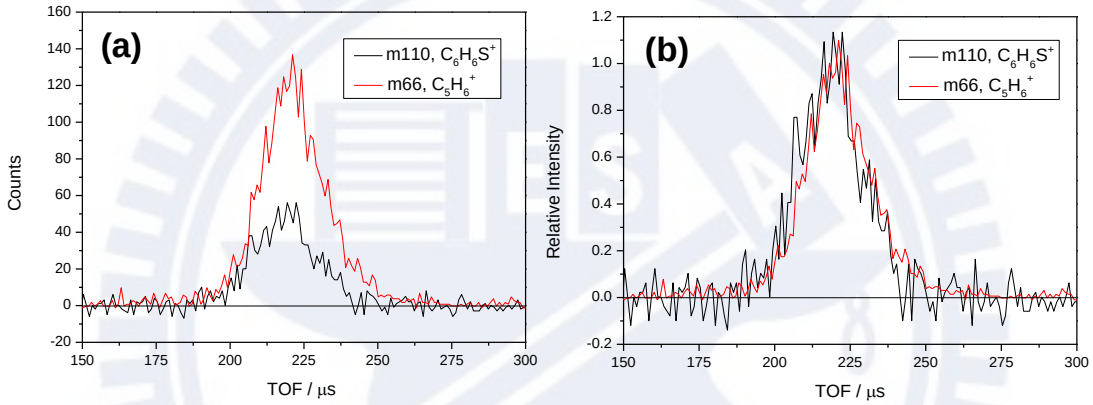

Figure 3-14 (a) TOF spectra and **(b)** Scaled TOF spectra of $C_6H_6S^+$ (m110 signal) and $C_5H_6^+$ (m66 signal) at 63°. The time zero was set at the beginning of the discharge interval, and the ion flight time is removed here. Before the S atomic beam intercepts with the C_6H_6 beam, the S atoms fly through 85 mm distance and it takes 71 μs for the flight.

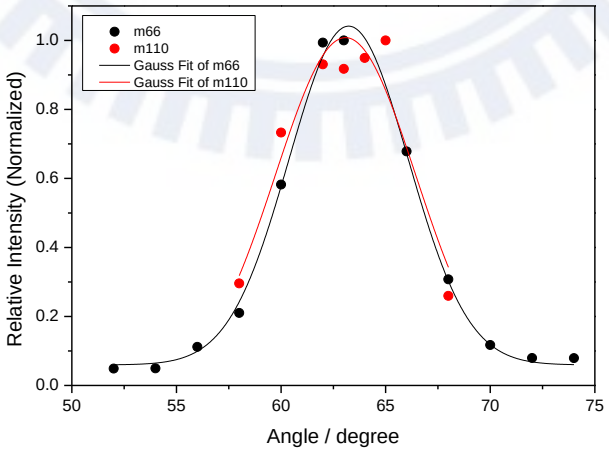

Figure 3-15 Angular distributions of $C_5H_6^+$ (m66 signal) and $C_6H_6S^+$ (m110 signal). The angle with the most intense signal is 63° for both m66 and m110 signals, and FWHM of the angular distributions for both signals are about 7°.

Figure 3-15 is the angular distributions of $C_5H_6^+$ and $C_6H_6S^+$. After optimization by Gauss curve, we can find out the most intense signal is at 63° for both products. This angle is what we used for Newton diagram shown in the beginning of Section 3.1.2.

In this work, we measured the PIE curves for the most two abundant daughter ions, $C_5H_6^+$ (m66 signal) and $C_5H_5^+$ (m65 signal), as Figure 3-16 and Figure 3-17 show. Both of these two curves begin to rise around 8.5 eV.

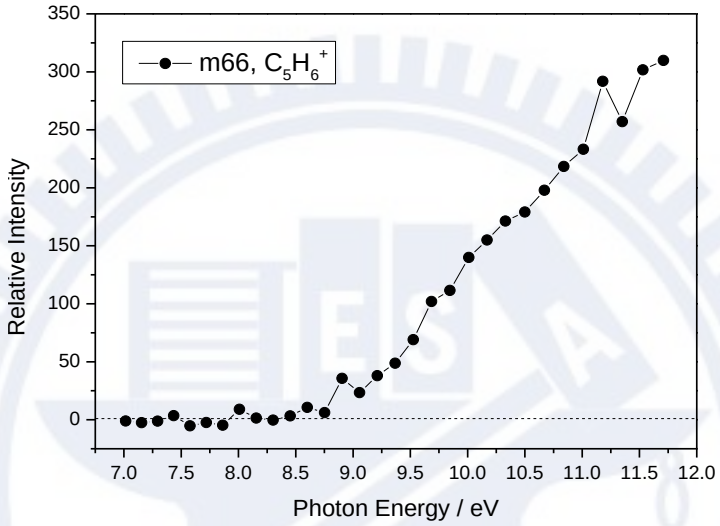

Figure 3-16 Photoionization efficiency curve of $C_5H_6^+$ (m66 signal) from S atom + C_6H_6 reaction

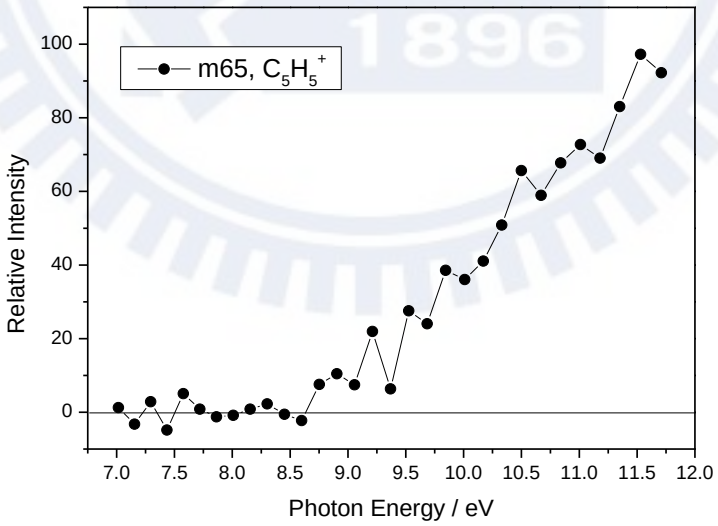

Figure 3-17 Photoionization efficiency curve of $C_5H_5^+$ (m65 signal) from S atom + C_6H_6 reaction

3.1.2-4 Formation of the C_6D_6S adduct from S atom + C_6D_6 crossed beam reaction

The reaction between S atom and C_6D_6 is fairly similar to that between S atom and C_6H_6. Figure 3-18 is the newton diagram for C_6D_6S adduct from the reaction between S atom and C_6D_6. Table 3.1 shows the parent and daughter ions of C_6D_6S and the comparison parts for C_6H_6S. Here, we focused on the parent and the daughter ions of C_6D_6S adduct, $C_6D_6S^+$ (m116 signal), $C_6D_5S^+$ (m114 signal), $C_5D_6^+$ (m72 signal) and $C_5D_5^+$ (m70 signal) in the center-of-mass angle 65°. The signal of $(C_6D_6)_2S$ might appear at lab angle 77°, and therefore we don't have to worry about the contributions from the daughter ions of $(C_6D_6)_2S$.

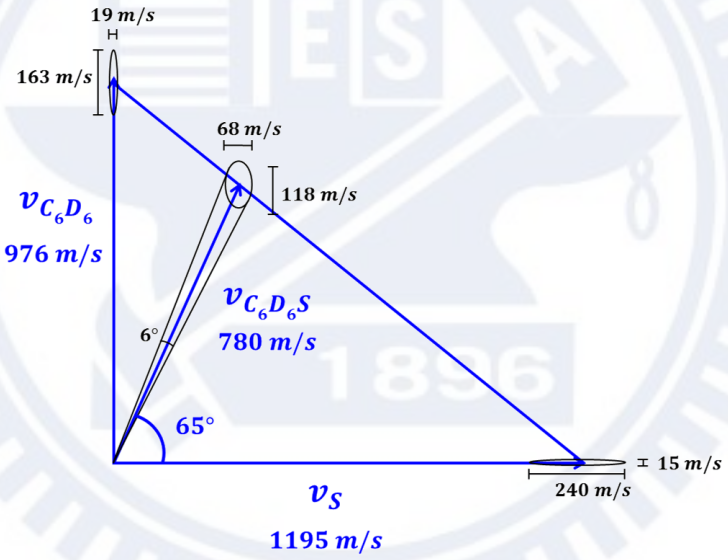

Figure 3-18 Newton diagram of the reaction between S atom and C_6D_6. The angle 65° is from the Gaussian fitting of the angular distribution data of $C_6D_6S^+$ (m116 product). The error bars of the C_6D_6 and S-atom velocities are calculated by matching the TOF spectra of C_6D_6 and S atom.

Table 3.1 Products of S + C_6H_6 reaction and the comparison products of S + C_6D_6 reaction

Mass	m116	m114	m72	m70
Ionic Species	$C_6D_6S^+$	$C_6D_5S^+$	$C_5D_6^+$	$C_5D_5^+$
Mass	m110	m109	m66	m65
Ionic Species	$C_6H_6S^+$	$C_6H_5S^+$	$C_5H_6^+$	$C_5H_5^+$

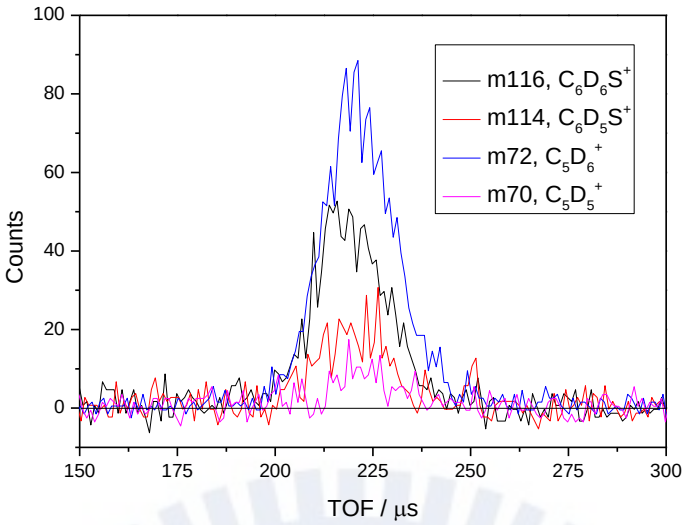

Figure 3-19 TOF spectra of m116, m114, m72 and m70 signals at 65°, which correspond to $C_6D_6S^+$, $C_6D_5S^+$, $C_5D_6^+$ and $C_5D_5^+$, respectively. (The curves are integration of 500k, 500k, 200k and 500k pulses for m116, m114, m72 and m70 signals, respectively) The ionizing photon energy is 11.35 eV. The time zero was set at the beginning of the discharge interval, and the ion flight time is removed here. Before the S atomic beam intercepts with the C_6D_6 beam, the S atoms fly through 85 mm distance (from the discharge position to the crossing point), and it takes 71 μs for the flight.

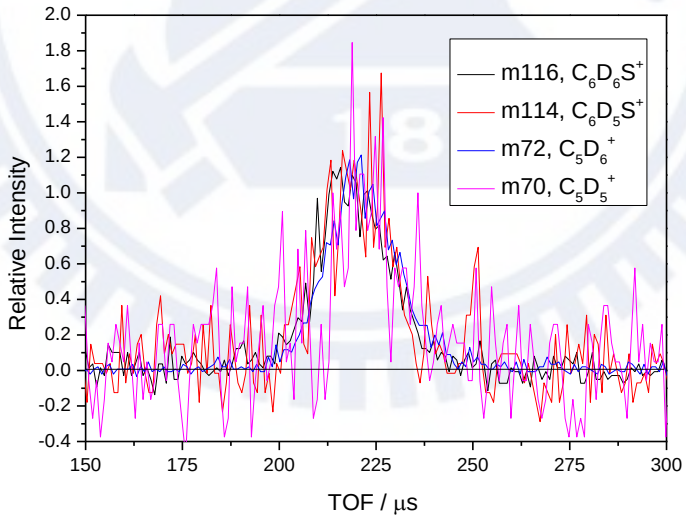

Figure 3-20 Scaled TOF spectra of $C_6D_6S^+$, $C_6D_5S^+$, $C_5D_6^+$ and $C_5D_5^+$ at 65°. The time zero was set at the beginning of the discharge interval, and the ion flight time is removed here. Before the S atomic beam intercepts with the C_6D_6 beam, the S atoms fly through 85 mm distance and it takes 71 μs for the flight.

Figure 3-19 shows TOF spectra of $C_6D_6S^+$, $C_6D_5S^+$, $C_5D_6^+$ and $C_5D_5^+$. After adjusting the ion flight time and removing background, the arrival time of these four ions are almost the same. Figure 3-20 is the scaled TOF of these four products, in which the distributions of these four products fit well with each other. Figure 3-19 and Figure 3-20 are the evidence that C_6D_6S is the only product formed at crossing point. $C_6D_6S^+$, $C_6D_5S^+$, $C_5D_6^+$ and $C_5D_5^+$ all generated from the neutral C_6D_6S adduct during ionization process. The lifetime is calculated to be of 128 μs. The results are quite similar to those in S atom + C_6H_6 reaction.

As what we did in 3.1.2-4, we measured angular distribution of the daughter ion which has the highest intensity to represent the behavior of C_6D_6S adduct, and thus $C_5D_6^+$ is measured here. Figure 3-21 shows the averaged value and the standard deviation of four sets of angular distributions of $C_5D_6^+$. The optimization angle is used for the Newton diagram of C_6D_6 + S reaction.

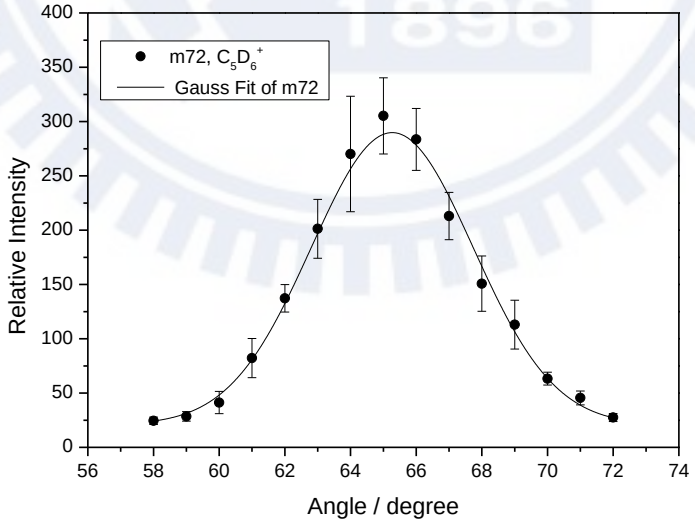

Figure 3-21 Averaged Angular Distribution of $C_5D_6^+$(m72 signal). After optimization, the angle with the most intense signal appears is 65°. FWHM of the angular distribution is 6°.

Figure 3-22 and Figure 3-23 are the PIE curves of $C_5D_6^+$and $C_6D_6S^+$, respectively. The appearance energy of $C_5D_6^+$ is around 8.5 eV, which is close to the value of $C_5H_6^+$ and $C_5H_5^+$ in S atom and C_6H_6 reaction (as Figure 3-16 and Figure 3-17 show). The ionization energy of C_6D_6S adduct is much lower than this value, around 7.75 eV. This result is quite reasonable because extra energy is required to break bonds to form daughter ions like $C_5D_6^+$.

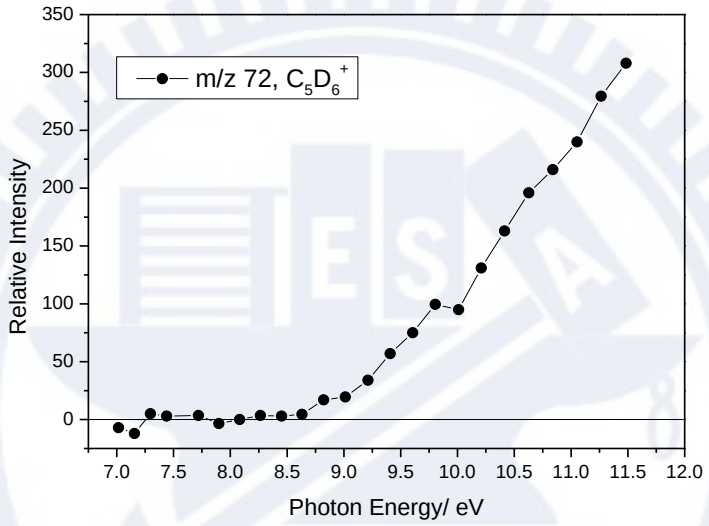

Figure 3-22 Photoionization efficiency curve of $C_5D_6^+$ (m72 signal) from S atom + C_6D_6 reaction

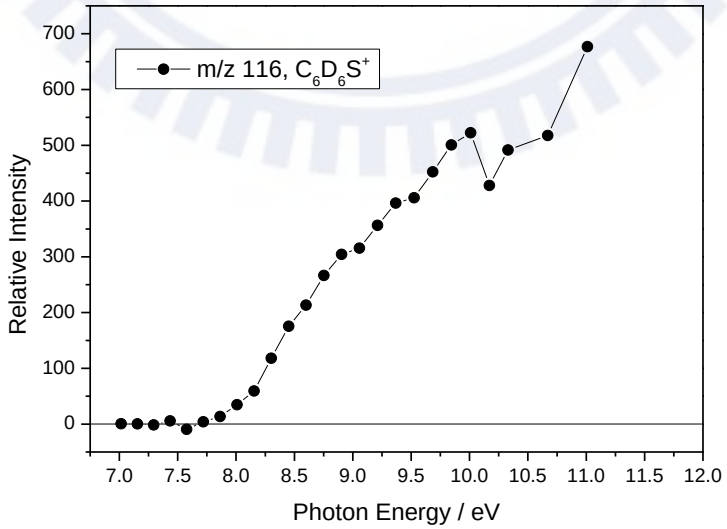

Figure 3-23 Photoionization efficiency curve of $C_6D_6S^+$ (m116 signal) from S atom + C_6D_6 reaction

3.1.3 C_6H_5SH (Thiophenol)

In this section, thiophenol (C_6H_5SH, ≥99% Sigma-Aldrich) liquid sample is examined. Thiophenol in Ne is used as molecular beam source of 90° pulsed valve, and Ne is used as that of 0° pulsed valve. The angular distribution of thiophenol is shown as Figure 3-24.

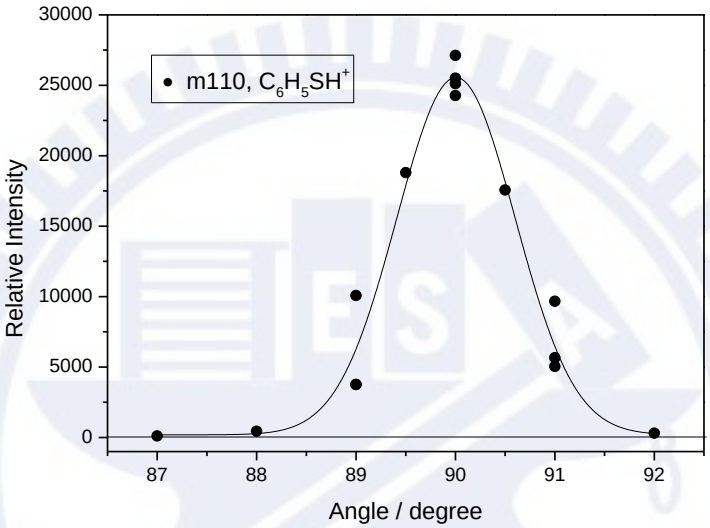

Figure 3-24 Angular distribution of $C_6H_5SH^+$ (m110 signal) of thiophenol sample. After optimization, the most intense signal appears at 90°, and the FWHM is found to be 1.4°.

The following is the PIE curves of $C_6H_5SH^+$ (m110 signal), as shown in Figure 3-25. The ionization energy of C_6H_5SH is near 8.3 eV. Compared to the ionization energy of C_6D_6S (m116 signal) from S + C_6D_6 reaction in Figure 3-23, the ionization energy of C_6H_5SH (m110 signal) from thiophenol sample is 0.75 eV higher. However, isotope effect does not make so much difference in ionization energy. It might result from higher internal energy of C_6D_6S adduct. Because C_6D_6S adduct has higher internal energy, less energy is required to ionize C_6D_6S adduct than thiophenol sample.

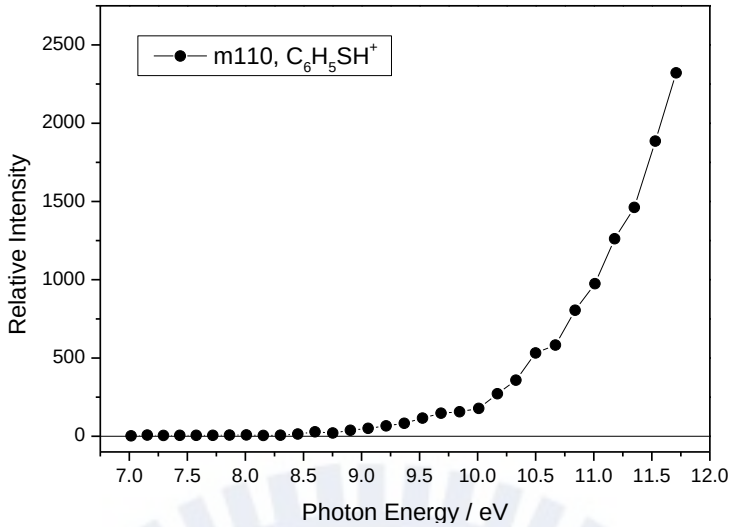

Figure 3-25 Photoionization efficiency curve of $C_6H_5SH^+$ (m110 signal) from thiophenol sample

Figure 3-26 shows the ratios of different ions generated from thiophenol sample during ionization process. We can find out thiophenol sample forms few daughter ions during ionization process. Even with higher photon energy, $C_6D_6S^+$ is still the dominant ions.

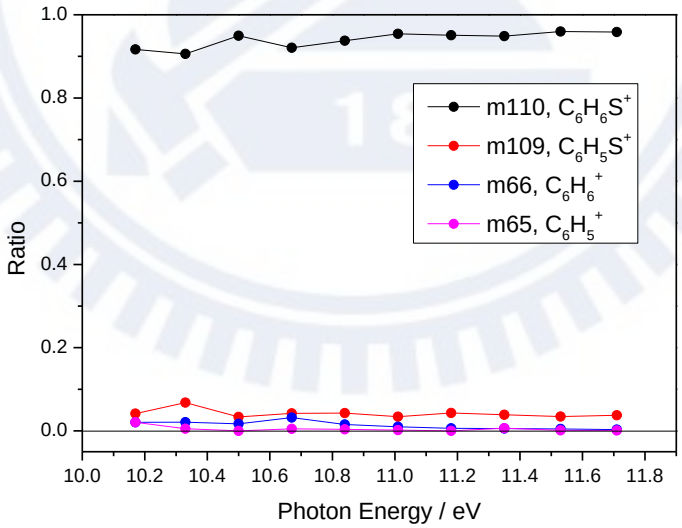

Figure 3-26 Ratios of $C_6D_6S^+$, $C_6D_5S^+$, $C_5D_6^+$ and $C_5D_5^+$ ions from thiophenol sample at different photon energies (calculated from PIE curves of these signals)

Figure 3-27 compares the relative intensities of parent and daughter ions from thiophenol sample to those from S + C_6D_6 reaction. The ratios of daughter ions to parent ions are much larger for C_6D_6S adduct than thiophenol sample. Fragments seemed to be generated more easily for C_6D_6S adduct, which indicates C_6D_6S adduct from S + C_6D_6 reaction has higher internal energy than thiophenol sample.

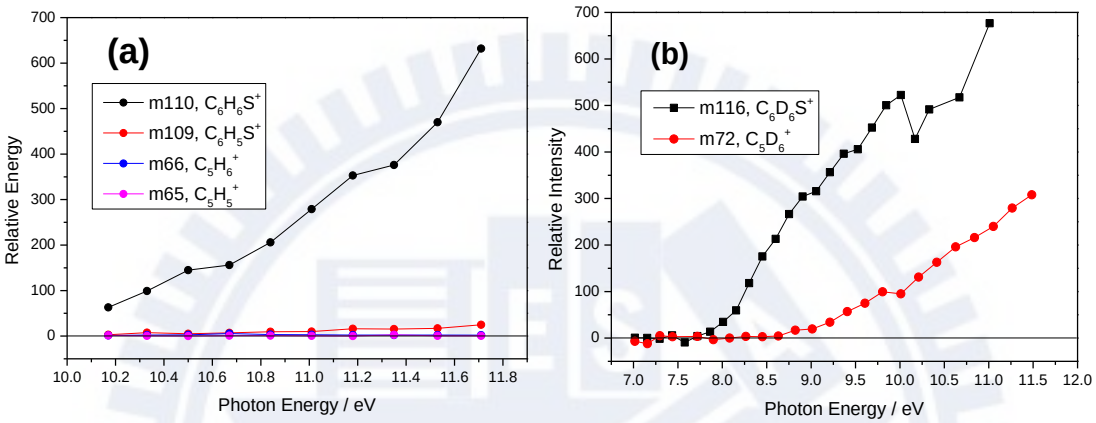

Figure 3-27 (a) Relative intensities of $C_6D_6S^+$, $C_6D_5S^+$, $C_5D_6^+$ and $C_5D_5^+$ ions from thiophenol sample at different photon energies **(b)** Relative intensities of $C_6D_6S^+$ and $C_5D_6^+$ ions from S + C_6D_6 reaction at different photon energies.

3.2 Results from Theoretical Calculations

3.2.1 Energy Diagram of $S(^3P) + C_6H_6$ reaction

All the intermediates and transition states are first optimized at B3LYP/6-311G(d,p) level of theory, and then re-optimized with aug-cc-pVTZ basis set for better geometries. Figure 3-28 is the energy diagram of stationary points calculated at B3LYP /aug-cc-pVTZ level of theory, in which the zero point energies (ZPE) have been included. The label "T" stands for intermediates on triplet potential energy surface, "S" for intermediates on singlet surface and "TS" for transition states. The geometries of intermediates and transition states are shown in Figure 3-29 and Figure 3-30, respectively.

By calculation, $S(^3P)$ atom initially reacts with C_6H_6 to form C_6H_6S diradical (T1) on triplet potential energy surface. It is an endothermic reaction with 7.1 kcal/mol barrier, which is quite different from $O(^3P) + C_6H_6$ reaction. Formation of C_6H_6O diradical is reported to be an exothermic reaction[1], and the relative energy of C_6H_6O diradical is -14.5 kcal/mol compared to $O(^3P) + C_6H_6$ reactants at CBS-QB3 level[1]. However, the collision energy of $S(^3P) + C_6H_6$ reaction is calculated to be 14.2 kcal/mol in our crossed beam experiments. Forming C_6H_6S diradical is thus energetically feasible.

Most intermediates of C_6H_6S formula are found to have lower energies in the singlet state rather than in the triplet state. Singlet state seems to be the ground state of most isomers, and therefore we put more emphasis on singlet potential energy surface. In section 3.2.2, we will discuss the possible path related to formation of singlet isomers through triplet-singlet intersystem crossing near the diradical geometry. In this section, we mainly focus on the reaction paths on singlet potential energy surface.

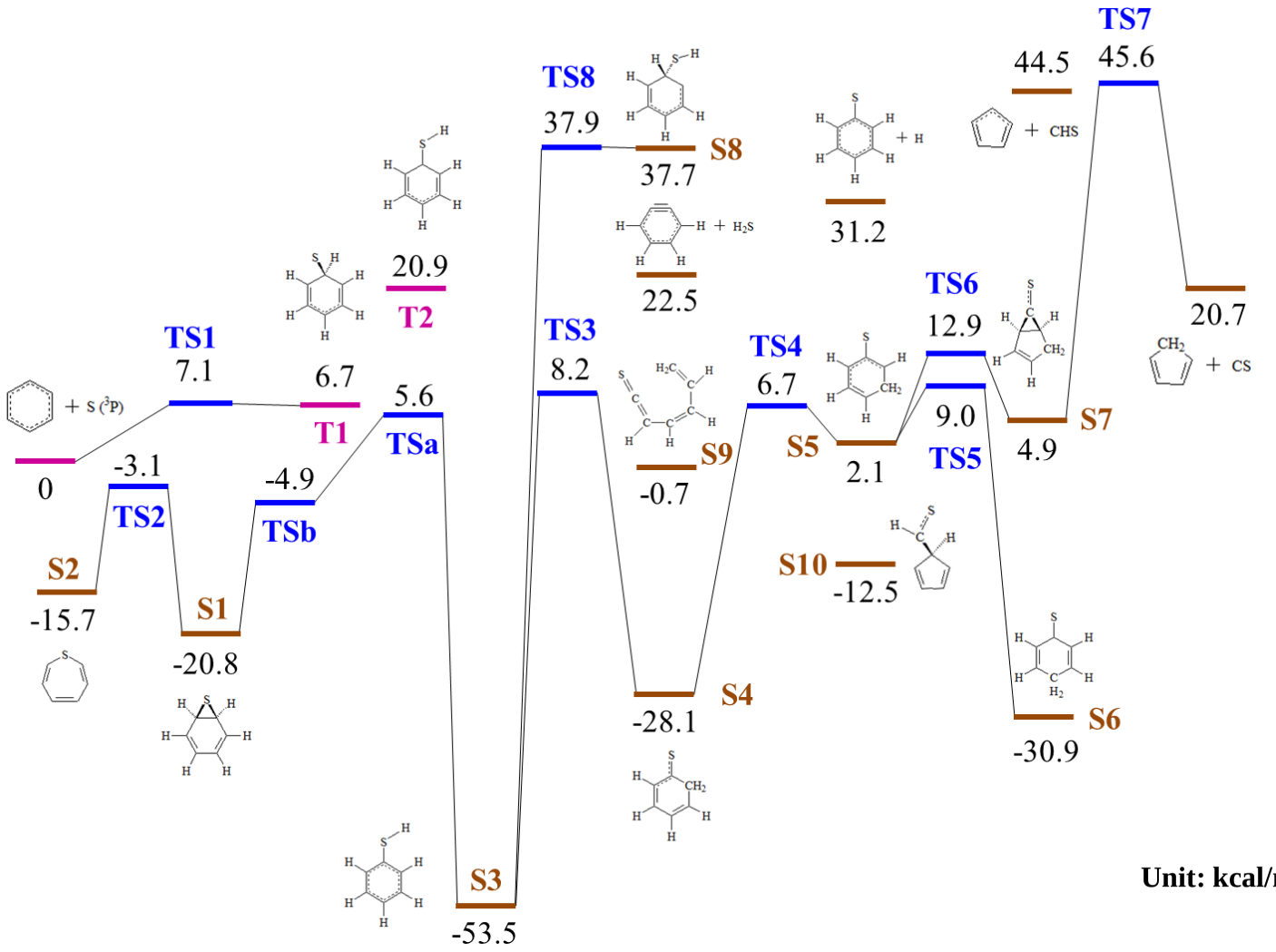

Figure 3-28 Energy diagram for S(^{3}P)+C_6H_6 reaction at B3LYP/aug-cc-PVTZ level of theory (ZPE included, Frequency Scale factor=0.97[27])

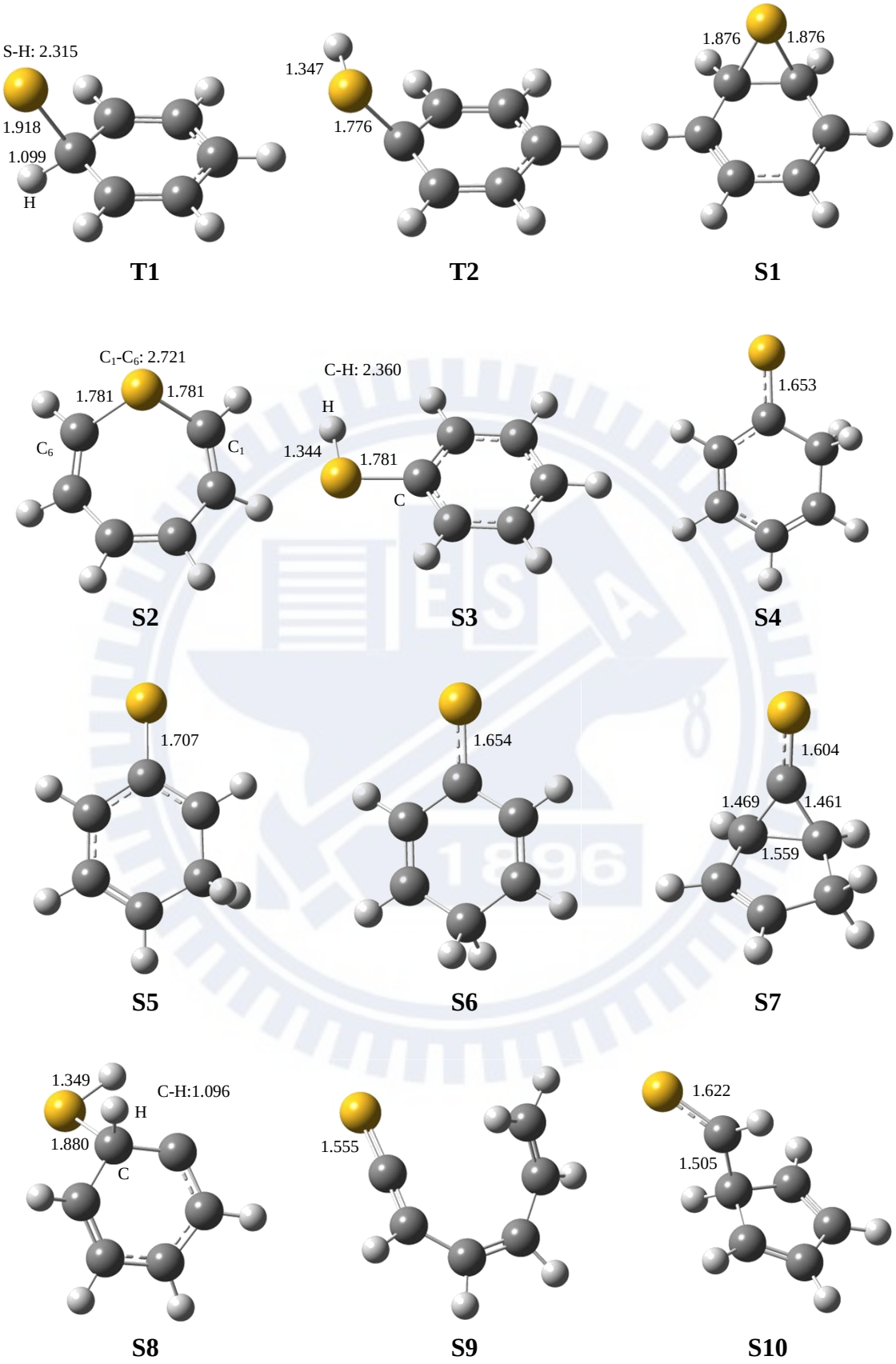

Figure 3-29 Optimized geometries of intermediates at B3LYP / aug-cc-pVTZ level

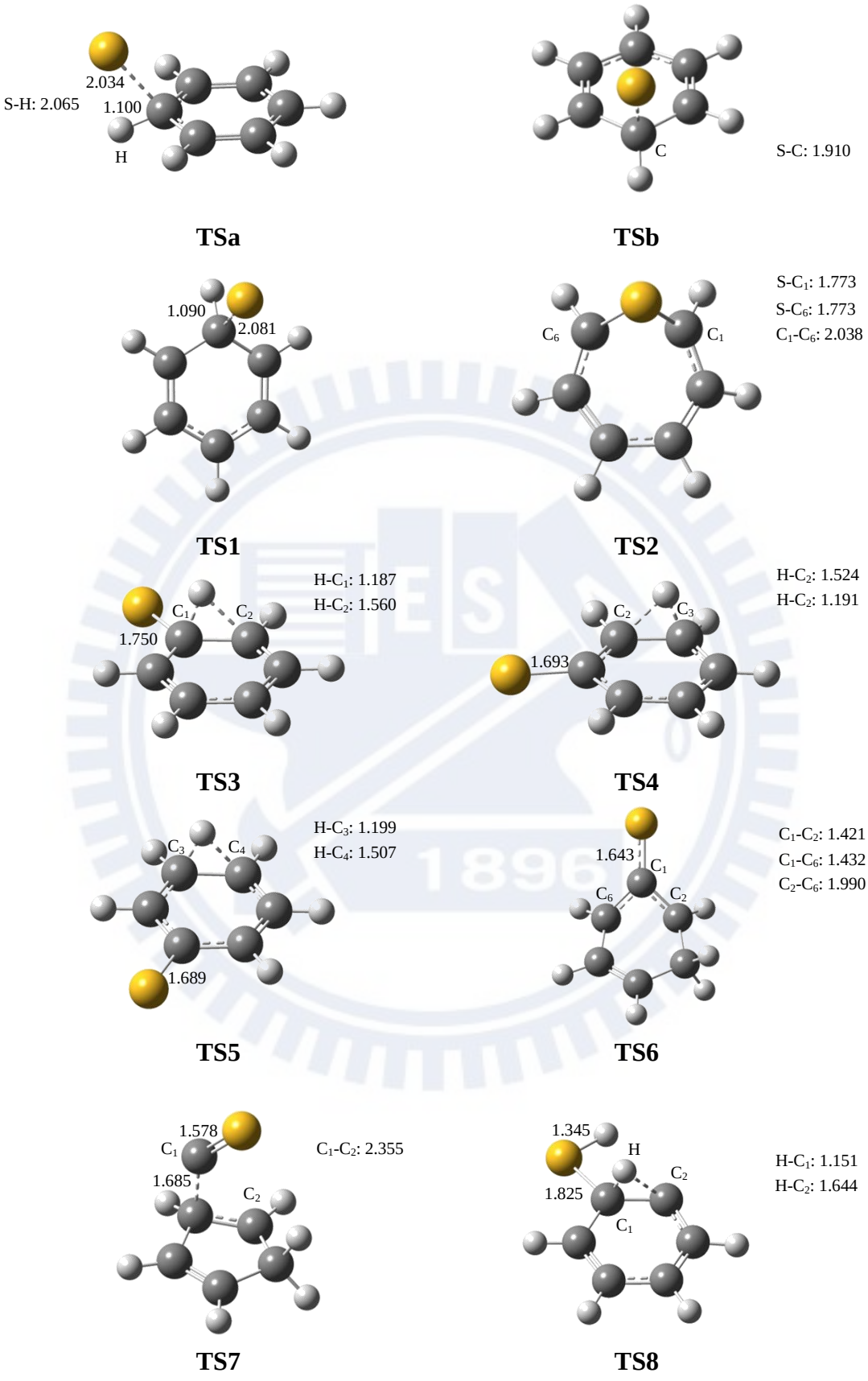

Figure 3-30 Optimized geometries of transition states at B3LYP / aug-cc-pVTZ level

Figure 3-31 shows the reaction paths on singlet potential energy surface. Benzene sulfide (S1) and thiophenol (S3) are found to be the main intermediates formed after intersystem crossing (see Section 3.2.2 for details). These two intermediates may further isomerize to other singlet isomers.

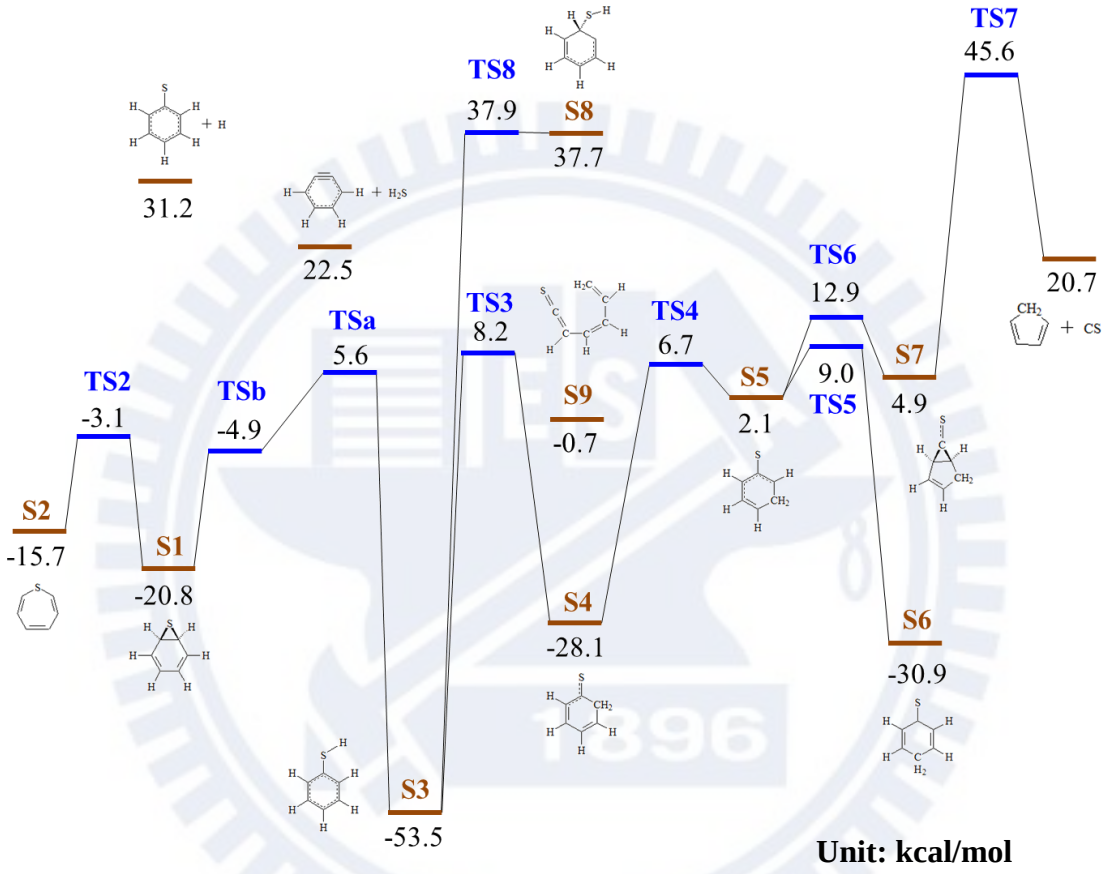

Figure 3-31 Energy diagram on singlet potential energy surface at B3LYP/aug-cc-pVTZ level of theory (ZPE included, frequency scale factor=0.97 [27]) Zero of energy here is $S(^3P) + C_6H_6$.

Benzene sulfide forms seven-membered-ring isomer, thiepine (S2) through a 17.7 kcal/mol barrier. This barrier is higher than the benzene oxide/Oxepin equilibrium, which is calculated to be 4.8 kcal/mol at CBS-QB3 level[1].

Benzyne and H_2S are formed from decomposition of thiophenol. Al-Muhtaseb et al.[12] have done the calculation on this path and regarded this channel to be of negligible importance. Therefore, we only calculate the enthalpy of benzyne + H_2S products to

show the relative energy compared to thiophenol, as Figure 3-31 shows. This value is only 0.4 kcal/mol lower than that calculated by Al-Muhtaseb et al.[12] at QCSID(T)/ 6-311+G(2d,p)// MP2/6-31G(d,p) level.

Hydrogen migration plays an important role in forming other isomers from thiophenol. Migration of H atom from S atom to β-carbon of thiophenol forms cyclohexa-2,4-dienethione (S4). β-hydrogen of S4 can further migrate to γ-carbon to form cyclohexa-1,3-dienethione (S5). S5 locates at a shallow local minimum. The energy differences between the transition states (TS4, TS6) and S5 are small, which makes S5 an unstable intermediate. S5 can forms S4 or cyclohexa-2,5-dienethione (S6) by H migration, or forms S7 intermediate by interaction between two carbons on either side of α-carbon. The barrier for decomposition of S7 into cyclopentadiene + CS is quite high relative to 14.2 kcal/mol total kinetic energy in the crossed beam experiments. This result also matches with the data from crossed beam experiment which show the observed m66 product at 63° is not from decomposition of m110 product before ionization.

Besides, another hydrogen migration channel is first found by calculation. Migration of H atom from β-carbon to α-carbon of thiophenol forms S8 intermediate. However, he energy of S8 is inaccessible under our experimental collision energy.

The enthalpy of phenylthio radical + H is also calculated. The energy difference relative to reactants is 31.2 kcal/mol. This high energy also makes formation of phenylthio radical (m109) impossible in the crossed beam experiments.

3.2.2 Intersystem Crossing from Triplet to Singlet Potential Energy Surface

As mentioned in section 3.2.1, the reactants $S(^3P)+C_6H_6$ are initially on the triplet potential energy surface, but most isomers of lower energies are on the singlet potential energy surface. We proposed intersystem crossing happens near the triplet diradical geometry and further forms singlet isomers.

Figure 3-32 shows the singlet intrinsic-reaction-coordinate (IRC) path for the transition state (TSa) which connects to thiophenol (S3) and benzene sulfide (S1). Optimization from the geometry of the 1st IRC step gives thiophenol (S3) and from the final step, it leads to benzene sulfide (S1). Transition state TSa is the geometry of the 51st step. TSb is the structure obtained from transition-state optimization (OPT=TS) from geometries of the 59th to 76th steps.

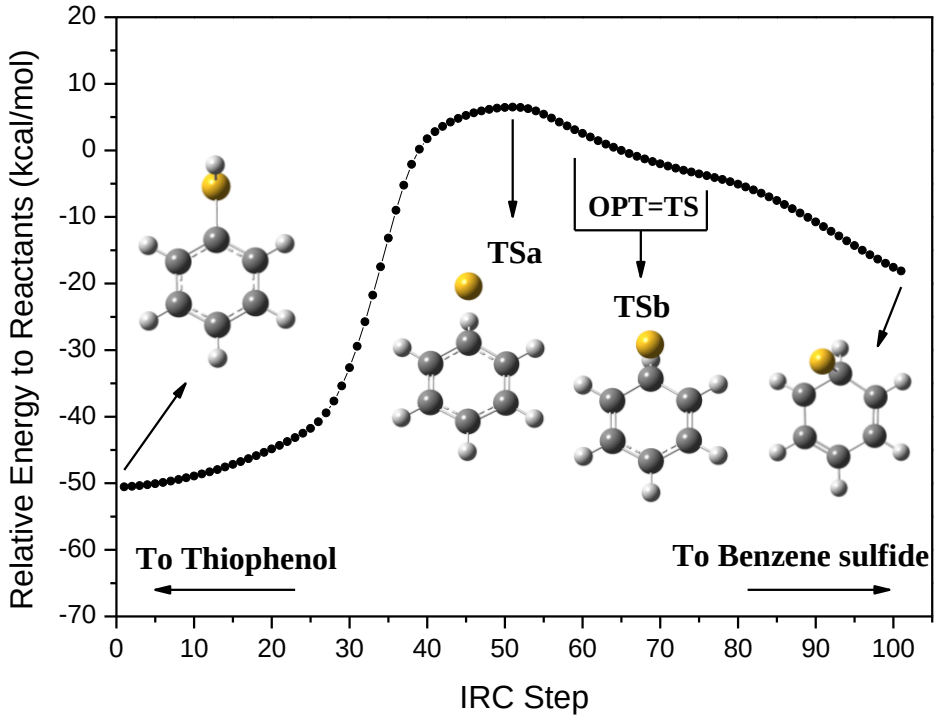

Figure 3-32 IRC path for S3–TSa–S1. The path is calculated at B3LYP/6-311G(d,p) level. (Relative energy is the energy compared to the reactants, and ZPE is not included.) Note that optimization of the geometries from the 59th to 76th step all leads to TSb structure.

The geometries and relative energies of TSa, TSb and related intermediates are listed in Table 3.2. The geometry of optimized triplet diradical (T1) is also shown. We found the geometry of the triplet diradical (T1) is in between those of TSa and TSb, and the energy of it is very close to TSa. Therefore, it is likely that intersystem crossing occurs around this region.

Table 3.2 Comparison of energies and geometries of stationary points calculated at B3LYP/6-311G(d,p) level

	Thiophenol	TSa	Diradical	TSb	Benzene sulfide
Spin	Singlet	Singlet	Triplet	Singlet	Singlet
C-S bond (Å)	1.79	2.03	1.94	1.91	1.88
S-C-H angle		78°	96°	111°	
C-H bond (Å)	2.36	1.10	1.10	1.09	1.08
S-H bond (Å)	1.35	2.09	2.33	2.52	2.48
Energy compared to reactants (kcal/mol) (with ZPE)	-51.61	5.98	6.84	-4.53	-20.07

To verify the above hypothesis, we calculated the excited-state energies of selected geometries along the IRC path in Figure 3-32 with time-dependent density functional method, TD-M06. The results are shown in Figure 3-33 and Figure 3-34. The solid circles show the ground state energies of the IRC path. Solid circles indicate the singlet states, and hollow circles indicate triplet ones. In Figure 3-34, we can see that the energy gap between the first excited state (triplet) and the ground state of thiophenol (S3) is larger than that of benzene sulfide (S1). First triplet excited state (red line) intercepts with ground state in the region of 49^{th}-62^{th} IRC steps; the energy of second triplet excited state (blue line) is close to that of the singlet ground state, and the closest point is the 54^{th} point. This region is also where we found the geometries are quite close to triplet diradical (T1) in Figure 3-32. Therefore, there might be singlet-triplet intersystem crossing occurring in this region.

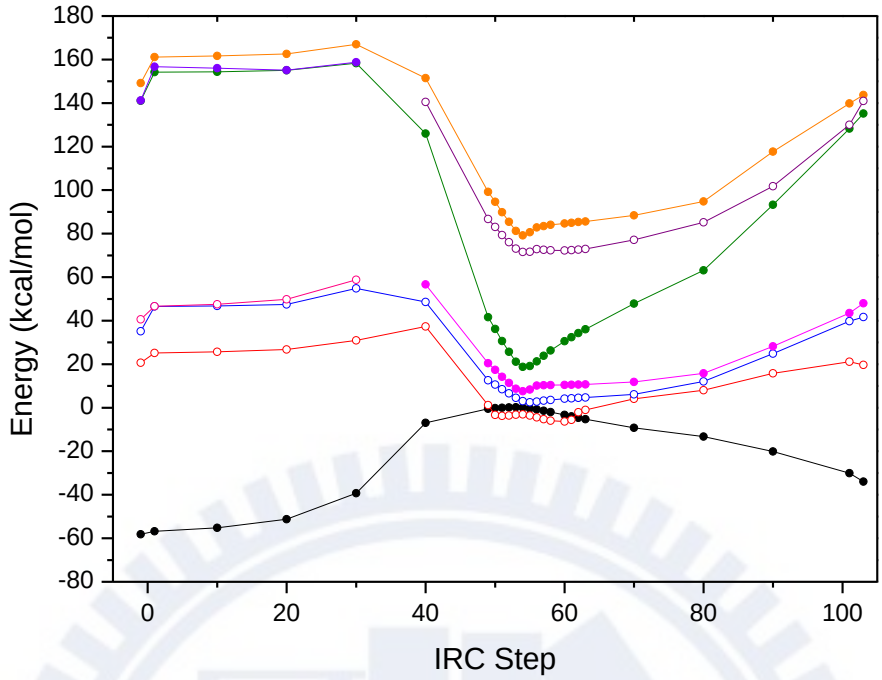

Figure 3-33 Ground and excited states along the IRC path in Figure 3-32 calculated at TD-M06/aug-cc-pVTZ//B3LYP/6-311G(d,p) level (without ZPE). Solid circles indicate singlet states, and hollow circles indicate triplet states. The energy of TSa ground state is set as the energy reference. The first and last points are the energy values of thiophenol (S3) and benzene sulfide (S1), respectively.

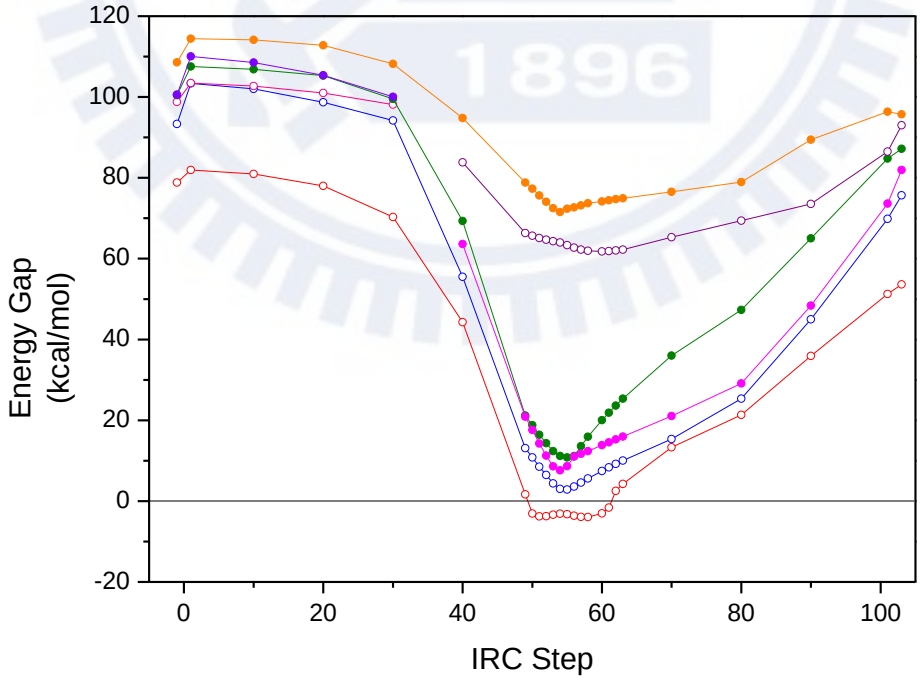

Figure 3-34 Energy difference of excited states relative to the ground state along the IRC path at TD-M06/aug-cc-pVTZ// B3LYP/6-311G(d,p) level.

We can find out on singlet potential energy surface the energies near crossing region are higher than its surroundings; on the contrary, crossing region on triplet potential energy surface is the local minimum. Therefore, it makes sense that we can only find out optimized triplet diradical intermediate because the singlet diradical is not stable and forms into other intermediates with lower energy, like thiophenol (S3) and benzene sulfide (S1).

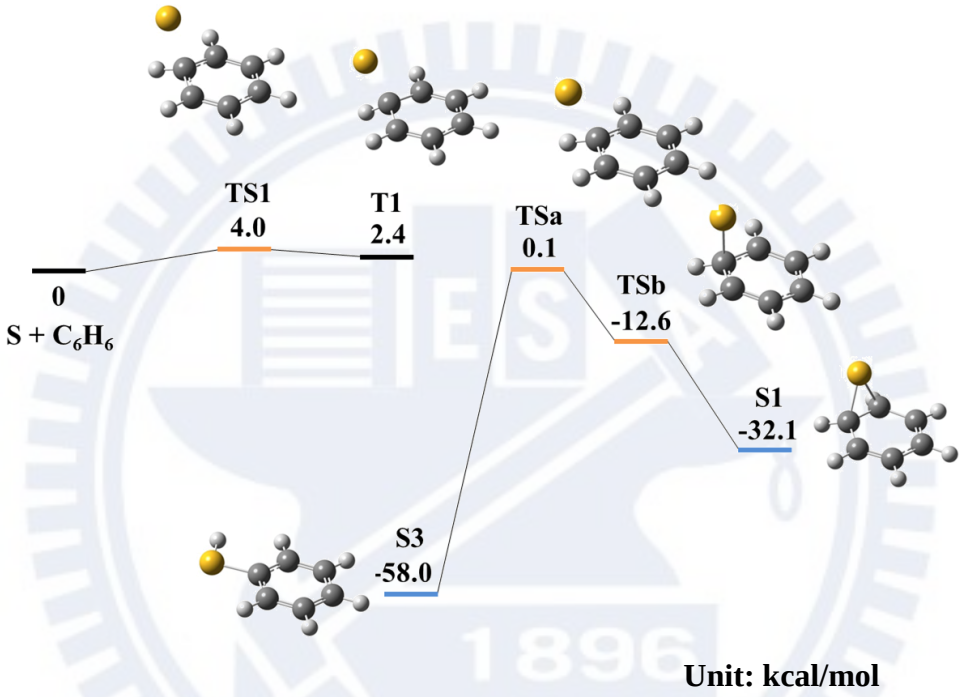

Figure 3-35 Energy diagram of stationary points near the singlet-triplet crossing region calculated at M06/aug-cc-pVTZ level. (ZPE included, Frequency scale factor =0.984[28])

M06 is regarded to have better performance on molecules composed by main group atoms. Therefore, we used M06/aug-cc-pVTZ method to optimize the stationary points near the crossing region to get more accurate energies, as Figure 3-35 shows. The largest difference between Figure 3-35 and Figure 3-28 is the energy of benzene sulfide, which decreases by a lot compared to other intermediates. However, the whole diagram keeps almost the same tendencies as those calculated by B3LYP method.

Chapter IV Summary

In this work, the $O(^3P)+C_6D_6$ crossed beam experiments have been reinvestigated with Synchrotron Radiation for better resolution. Long-lived C_6D_6O adducts has been detected at the angle of center-of-mass with only 6° FWHM of angular distribution. Based on TOF spectra and angular distributions, the measured $C_6D_5O^+$, $C_6D_5O^+$, $C_5D_6^+$ and $C_5D_5^+$ ions are the parent and daughter ions of the neutral C_6D_6O adduct.

The crossed beam experiments of $S(^3P)+C_6H_6$ and $S(^3P)+C_6D_6$ are reported for the first time. Based on TOF spectra and angular distributions, long-lived hot adducts C_6H_6S and C_6D_6S are formed at the angle of the center of mass, indicating zero recoil velocity. PIE curves of the C_6D_6S adduct and thiophenol sample were measured. From the PIE curves, lower ionization energy and more fragmentation are observed for the C_6D_6S adduct, indicating this adduct has higher internal energy than the thiophenol sample. Although the observed C_6D_6O, C_6D_6S and C_6D_6S adducts have high internal energy and are thermodynamically unstable, their lifetimes may exceed the experimental time of flight which is in the order of hundreds of microseconds before the adducts are ionized.

Theoretical calculations on the $S(^3P) + C_6H_6$ reaction are also performed in this work. Geometry optimization of stationary points and intrinsic reaction paths (IRC) are carried out with B3LYP method. From the IRC data, we proposed that $S(^3P) + C_6H_6$ initially forms triplet C_6H_6S diradical, which may form either singlet thiophenol or singlet benzene sulfide through intersystem crossing near the diradical geometry. Thiophenol or benzene sulfide may undergo further isomerization to form other products. However we find that most dissociation pathways on the singlet surface is much higher in energy than $S(^3P) + C_6H_6$ asymptote, thus giving support to the large life time of the adduct. Furthermore, energies of ground state and excited states near the intersystem crossing region are calculated by time-dependent density functional methods (TD-M06). The results show the energies of ground state and the first triplet excited state are really close or even the same near the diradical geometry. The geometries of stationary points near the crossing region are reoptimized at M06/aug-cc-pVTZ level for better accuracy.

Reference

1. Nguyen, T. L.; Peeters, J.; Vereecken, L. *Journal of Physical Chemistry A* **2007**, *111*, 3836 – 3849.
2. Taatjes, C. A.; Osborn, D. L.; Selby, T. M.; Meloni, G; Trevitt, A. J.; Epifanovsky, E.; Krylov, A. I.; Sirjean, S.; Dames, E.; Wang ,H. *Journal of Physical Chemistry A* **2010**, *114*, 3355–3370.
3. Sibener, S. J.; Buss, R. J.; Casavecchia, P.; Hirooka, T.; Lee, Y. T. *Journal of Chemical Physics* **1980**, 72, 4341.
4. Bajaj, P. N.; Fontijn, A. *Combustion and Flame* **1996**, *105*, 239.
5. Parker, J. K.; Davis, S. R. *Journal of the American Chemical Society* **1999**, *121*, 4271.
6. Tsuchiya, K.; Yamashita, K.; Miyoshi, A.; Matsui, H. *Journal of Physical Chemistry* **1996**, *100*, 17202-17206.
7. Leonori, F.; Petrucci, R.; Balucani, N.; Hickson, K. M.; Hamberg, M.; Geppert, W. D.; Casavecchia, P. *Journal of Physical Chemistry A* **2009**, *113*, 4330–4339.
8. Leonori, F.; Petrucci, R.; Balucani, N.; Casavecchia, P.; Rosi, M.; Skouteris, D.; Berteloite, C.; Le Picard, S.; Canosa, A.; Sims, I. R. *Journal of Physical Chemistry A* **2009**, *113*, 15328–15345
9. Berteloite, C.; Le Picard, S. D.; Sims, I. R.; Rosi, M.; Leonori, F.; Petrucci, R.; Balucani, N,; Wang, X.; Casavecchia, P. *Physical Chemistry Chemical Physics* **2011**, *13*, 8485–8501.
10. Lim, I. S.; Lim, J. S.; Lee, Y. S.; Kim, S. K. *Journal of Chemical Physics* **2007**, *126*, 034306.
11. Lim, J. S.; Choi, H.; Lim, I. S.; Park, S. B.; Lee, Y. S.; Kim,S. K. *Journal of Physical Chemistry A* **2009**, *113*, 10410–10416.
12. Al-Muhtaseb, A. H.; Altarawneh, M.; Almatarneh, M. H.; Poirier, R. A.; Assaf, N. W. *Journal of Computational Chemistry* **2011**, *32*, 2708–2715.
13. Lee, S. H.; Chen,W. K.; Huang, W. J. *Journal of Chemical Physics* **2009**, *130*, 054301.
14. Lu, C. W.; Wu,Y. J.; Lee, Y. P.; Zhu, R. S. ; Lin, M. C. *Journal of Chemical Physics* **2006**, *125*, 164329.
15. Wu, C.Y.R.; Chen, F.Z.; Judge, D.L. *Journal of Quantitative Spectroscopy and Radiative Transfer* **1999**, *61(2)*, 265—271.
16. Huang, W. J.; Chaudhuri, C.; Chen, W. K.; Lee, S. H. *Review of Scientific Instruments* **2007**, *78*, 083103.

17. Gaussian 09, Revision A.02, Frisch, M. J.; Trucks, G. W.; Schlegel, H. B.; et al., Gaussian, Inc., Wallingford CT, 2009.
18. Becke, A. D. *Journal of Chemical Physics* **1993**, *98*, 5648.
19. Stevens, P. J.; Devlin, F. J.; Chablowski, C. F.; Frisch, M. J. *Journal of Physical Chemistry* **1994**, *98*, 11623.
20. Kendall, R. A.; Dunning Jr., T. H.; Harrison, R. J. *Journal of Chemical Physics*, **1992**, *96*, 6796-806.
21. Zhao, Y.; Truhlar, D. G. *Journal of Chemical Physics* **2006**, ***125***, 194101.
22. NIST Chemistry WebBook, 2005.
23. Lee, S. H.; Lin, J. J.; Lee, Y. T. *Journal of Electron Spectroscopy and Related Phenomena* **2005**, *144–147*, 135–138.
24. Davidson, J. A.; Sadowski, C. M.; Schiff, H. I.; Streit, G. E.; Howard, C. J. Jennings, D. A.; Schmeltekopf, A. L. *Journal of Chemical Physics* **1976**, *64*, 57.
25. Person, J. C. *Journal of Chemical Physics* **1965**, *43*, 2553.
26. Pan, W. C.; Chen, I. C.; Huang, T. P.; Yuh, J. Y.; Lee, Y. Y. *Journal of Chemical Physics* **2008**, *129*, 134305.
27. NIST Computational Chemistry Comparison and Benchmark Database,
NIST Standard Reference Database Number 101
Release 15b, August 2011, Editor: Russell D. Johnson III
http://cccbdb.nist.gov/
28. Alecu, I. M.; Zheng, J.; Zhao, Y.; Truhlar, D. G. *Journal of Chemical Theory and Computation* **2010**, *6*, 2872–2887

Appendix

Optimized Geometries and Energies for Stationary Points of the $S(^3P) + C_6H_6$ Reaction in this Work

T1

B3LYP/ aug-cc-pVTZ

Atom	Coordinates (Angs)		
	X	Y	Z
C	-2.086093	0.000051	-0.42715
C	-1.450343	-1.219075	-0.1164
C	-0.204781	-1.244662	0.439995
C	-0.204671	1.244629	0.440013
C	-1.450243	1.219133	-0.116357
H	-3.069815	0.000089	-0.873967
H	-1.965550	-2.150941	-0.309985
H	0.276638	-2.180866	0.684414
H	0.276815	2.180801	0.684415
H	-1.965409	2.151027	-0.309923
C	0.563543	-0.000054	0.658421
H	1.077365	-0.000039	1.629483
S	2.147843	-0.000013	-0.423473

E(UB3LYP) (Hatree): -630.46290767

ZeroPoint Energy (Hatree): 0.09906

T2

B3LYP/ aug-cc-pVTZ

Atom	Coordinates (Angs)		
	X	Y	Z
C	0.555780	-0.017510	0.562423
C	-0.198184	1.250869	0.455634
C	-1.442468	1.244993	-0.091986
C	-2.087270	0.024041	-0.426563
C	-1.474614	-1.220914	-0.086644
C	-0.228462	-1.264495	0.44467
H	0.258225	2.170067	0.800847
H	-1.980124	2.177098	-0.216628
H	-3.081451	0.036913	-0.848208
H	-2.041937	-2.135652	-0.206312
H	0.211513	-2.200751	0.763956
S	2.093195	-0.085914	-0.323983
H	2.393974	1.225051	-0.255121

E(UB3LYP) (Hatree): -630.43634462

ZeroPoint Energy (Hatree): 0.0949829

S1

B3LYP/ aug-cc-pVTZ

Atom	Coordinates (Angs)		
	X	Y	Z
C	-0.391196	-1.707573	0.723605
C	-0.435121	-0.558831	1.421119
C	-0.435121	0.741159	0.744823
C	-0.435121	-0.558831	-1.421119
C	-0.391196	-1.707573	-0.723605
H	-0.389197	-2.656142	1.243032
H	-0.490926	-0.566432	2.501212
H	-0.945383	1.550379	1.248723
H	-0.490926	-0.566432	-2.501212
H	-0.389197	-2.656142	-1.243032
C	-0.435121	0.741159	-0.744823
H	-0.945383	1.550379	-1.248723
S	1.174267	1.352958	0

E(UB3LYP) (Hatree): -630.50939969

ZeroPoint Energy (Hatree): 0.1017437

S2

B3LYP/ aug-cc-pVTZ

Atom	Coordinates (Angs)		
	X	Y	Z
C	1.655452	0.674520	-0.27702
C	1.655452	-0.674520	-0.27702
C	0.656875	-1.550921	0.30405
C	0.656875	1.550921	0.30405
C	-0.665701	-1.360708	0.358826
C	-0.665702	1.360708	0.358826
H	2.545911	1.167517	-0.65135
H	2.545911	-1.167517	-0.65135
H	1.037085	-2.464119	0.753307
H	1.037085	2.464119	0.753307
H	-1.303403	-2.066056	0.876199
H	-1.303403	2.066056	0.876199
S	-1.519918	0.000000	-0.411661

E(UB3LYP) (Hatree): -630.49961221

ZeroPoint Energy (Hatree): 0.100041

S3

B3LYP/ aug-cc-pVTZ

Atom	Coordinates (Angs)		
	X	Y	Z
C	-0.505191	0.000688	0
C	0.200070	-1.203450	0.000001
C	1.588454	-1.196947	0
C	2.288855	0.004029	0
C	1.584994	1.202495	0
C	0.195780	1.206211	-0.000001
H	-0.335197	-2.143488	0.000003
H	2.123105	-2.137139	0.000001
H	3.369703	0.005899	0
H	2.116876	2.144368	-0.000001
H	-0.338026	2.146700	-0.000002
S	-2.283842	-0.083433	-0.000002
H	-2.512760	1.240425	0.000028

E(UB3LYP) (Hatree): -630.55899644

ZeroPoint Energy (Hatree): 0.0991902

S4

B3LYP/ aug-cc-pVTZ

Atom	Coordinates (Angs)		
	X	Y	Z
C	-2.251446	0.061373	-0.000058
C	-1.649365	-1.133966	-0.000036
C	0.639676	0.020424	0.000029
C	-0.103608	1.251540	0.000056
C	-1.458476	1.270435	0.00001
H	-3.329546	0.141983	-0.000124
H	-2.228943	-2.048288	-0.000078
H	0.463046	2.171681	0.000081
H	-1.973570	2.222593	0.000009
S	2.292267	0.001327	-0.000043
C	-0.161605	-1.265443	0.000075
H	0.150769	-1.867595	0.859889
H	0.150921	-1.867787	-0.859542

E(UB3LYP) (Hatree): -630.52013595

ZeroPoint Energy (Hatree): 0.1009283

S5

B3LYP/ aug-cc-pVTZ

Atom	Coordinates (Angs)		
	X	Y	Z
C	-0.100507	-1.173533	0.172696
C	0.649828	-0.000713	0.137617
C	-0.113848	1.203092	0.199635
C	-1.501766	1.256383	-0.028552
C	-2.227832	0.112762	-0.179581
H	0.406927	-2.120966	0.296647
H	0.430927	2.124115	0.360967
H	-1.985935	2.222569	-0.079909
H	-3.288752	0.132986	-0.382388
S	2.336821	-0.004318	-0.122452
C	-1.559279	-1.185841	-0.016741
H	-1.843843	-1.882082	-0.820322
H	-1.988029	-1.680439	0.873793

E(UB3LYP) (Hatree): -630.4700057

ZeroPoint Energy (Hatree): 0.0988562

S6

B3LYP/ aug-cc-pVTZ

Atom	Coordinates (Angs)		
	X	Y	Z
C	1.443720	-1.246894	0
C	0.103685	-1.237610	0
C	-0.661301	0.000000	0
C	0.103685	1.237610	0
C	1.443720	1.246894	0
H	1.977443	-2.189326	0
H	-0.459720	-2.160108	0
H	-0.459720	2.160108	0
H	1.977442	2.189326	0
S	-2.315737	0.000000	0
C	2.256821	0.000000	0
H	2.937177	0.000000	0.863165
H	2.937177	0.000000	-0.863164

E(UB3LYP) (Hatree): -630.52507571

ZeroPoint Energy (Hatree): 0.1013674

S7

B3LYP/ aug-cc-pVTZ

Atom	Coordinates (Angs)		
	X	Y	Z
C	1.484101	-1.160992	-0.175888
H	1.124471	-1.811127	-0.9777
H	2.269693	-1.711441	0.34893
C	-0.780772	-0.001516	0.250516
S	-2.259423	-0.015285	-0.372192
C	1.357949	1.203660	-0.146509
C	1.978539	0.164253	-0.698745
H	1.536498	2.242618	-0.382388
H	2.744339	0.237426	-1.457762
C	0.311273	0.785552	0.8383
H	0.142092	1.359509	1.741247
C	0.345162	-0.771848	0.772261
H	0.156164	-1.387081	1.643142

E(UB3LYP) (Hatree): -630.4668571

ZeroPoint Energy (Hatree): 0.1001033

S8

B3LYP/ aug-cc-pVTZ

Atom	Coordinates (Angs)		
	X	Y	Z
C	-1.519273	-1.237366	0.04437
C	-1.991838	-0.045569	-0.496599
C	-1.387344	1.204659	-0.190397
C	-0.217825	1.246684	0.488608
C	-0.189670	-1.298867	0.437129
H	-2.114461	-2.139717	-0.034498
H	-2.854268	-0.053240	-1.155138
H	-1.913192	2.113383	-0.451796
H	0.161725	2.170549	0.907611
C	0.515148	-0.022145	0.710897
H	0.912062	-0.055447	1.732033
S	2.021570	0.012609	-0.414091
H	2.207826	-1.321649	-0.336801

E(UB3LYP) (Hatree): -630.40983235

ZeroPoint Energy (Hatree): 0.0952872

S9

B3LYP/ aug-cc-pVTZ

Atom	Coordinates (Angs)		
	X	Y	Z
C	2.050560	-0.384685	-0.276669
C	1.793995	1.050683	-0.289258
C	-1.132643	-0.604091	0.065757
C	1.243505	-1.421945	0.020445
H	3.062928	-0.656038	-0.55803
H	2.369559	1.605929	-1.024311
H	1.707255	-2.400938	0.022916
C	1.013677	1.745342	0.542019
H	0.454369	1.277004	1.339354
H	0.934347	2.820300	0.457605
C	-0.181710	-1.479942	0.309685
H	-0.550067	-2.418840	0.716463
S	-2.293919	0.396276	-0.199117

E(UB3LYP) (Hatree): -630.47325247

ZeroPoint Energy (Hatree): 0.0975179

S10

B3LYP/ aug-cc-pVTZ

Atom	Coordinates (Angs)		
	X	Y	Z
C	1.055395	-1.177479	0.21884
C	1.055395	1.177479	0.21884
C	2.253281	0.730915	-0.196966
H	0.735906	-2.202708	0.317544
H	0.735905	2.202708	0.317544
H	3.095397	1.344124	-0.482442
C	2.253281	-0.730915	-0.196966
H	3.095397	-1.344124	-0.482442
C	0.156866	0.000000	0.513419
H	-0.206582	0.000000	1.543146
C	-1.011736	0.000000	-0.434268
H	-0.718550	0.000000	-1.483177
S	-2.582023	0.000000	-0.029223

E(UB3LYP) (Hatree): -630.4942739

ZeroPoint Energy (Hatree): 0.0999055

TS1

B3LYP/ aug-cc-pVTZ

Atom	Coordinates (Angs)		
	X	Y	Z
C	-2.042029	0.000006	-0.503209
C	-1.437727	-1.216281	-0.144555
C	-0.234248	-1.233456	0.511538
C	-0.234237	1.233451	0.511543
C	-1.437716	1.216288	-0.14455
H	-2.988734	0.000011	-1.024796
H	-1.936852	-2.148515	-0.373126
H	0.226045	-2.167354	0.800556
H	0.226063	2.167343	0.800565
H	-1.936834	2.148527	-0.373117
C	0.489213	-0.000006	0.764424
H	1.108092	-0.00001	1.66125
S	2.167667	-0.000001	-0.466405

E(UB3LYP) (Hatree): -630.46230447

ZeroPoint Energy (Hatree): 0.0989983

TS2

B3LYP/ aug-cc-pVTZ

Atom	Coordinates (Angs)		
	X	Y	Z
C	1.640412	0.700448	-0.342639
C	0.666009	1.457007	0.288512
C	-0.627855	1.019054	0.564878
C	0.666009	-1.457007	0.288512
C	1.640412	-0.700448	-0.342639
H	2.559364	1.193969	-0.632299
H	0.953441	2.417906	0.702606
H	-1.212128	1.498532	1.339349
H	0.95344	-2.417906	0.702606
H	2.559364	-1.193969	-0.632299
C	-0.627855	-1.019053	0.564878
H	-1.212127	-1.498531	1.33935
S	-1.546509	0	-0.55927

E(UB3LYP) (Hatree): -630.47877936

ZeroPoint Energy (Hatree): 0.0993207

TS3

B3LYP/ aug-cc-pVTZ

Atom	Coordinates (Angs)		
	X	Y	Z
C	0.601107	0.00618	0.030894
C	-0.187109	1.235071	0.023936
C	-1.55058	1.220798	-0.010662
C	-2.272081	0.005664	-0.040202
C	-1.595458	-1.19436	-0.027393
C	-0.198976	-1.221399	-0.012398
H	0.362714	2.165115	0.031923
H	-2.092135	2.157514	-0.022617
H	-3.352509	0.021819	-0.060894
H	-2.1355	-2.131179	-0.04544
H	0.350585	-2.151701	0.006957
S	2.348833	0.003412	-0.05167
H	0.504097	-0.427888	1.131745

E(UB3LYP) (Hatree): -630.45840474

ZeroPoint Energy (Hatree): 0.0968965

TS4

B3LYP/ aug-cc-pVTZ

Atom	Coordinates (Angs)		
	X	Y	Z
C	-2.265625	0.050178	-0.100101
C	-1.554088	-1.177012	-0.028363
C	0.651212	0.03616	0.045498
C	-0.145964	1.222998	0.082233
C	-1.53004	1.224473	-0.010634
H	-3.34065	0.050241	-0.186959
H	-2.053083	-2.113293	-0.248638
H	0.381591	2.164423	0.15145
H	-2.047928	2.174807	-0.018378
S	2.340846	0.00117	-0.048403
C	-0.097485	-1.171359	0.002004
H	-1.15911	-1.28671	1.089766
H	0.417592	-2.120818	0.043385

E(UB3LYP) (Hatree): -630.4613168

ZeroPoint Energy (Hatree): 0.0973608

TS5

B3LYP/ aug-cc-pVTZ

Atom	Coordinates (Angs)		
	X	Y	Z
C	-0.11304	-1.206162	-0.026761
C	0.65708	-0.01584	0.001089
C	-0.120469	1.202875	0.003774
C	-1.493666	1.252249	-0.014953
C	-2.250145	0.074316	-0.06259
H	0.400069	-2.15668	-0.040579
H	0.440465	2.127655	0.032081
H	-2.000984	2.207087	0.003557
H	-3.328814	0.065102	-0.085767
S	2.345585	0.000713	0.000567
C	-1.526101	-1.189985	-0.025884
H	-2.071819	-2.102652	-0.233294
H	-1.890223	-0.856636	1.066885

E(UB3LYP) (Hatree): -630.45734839

ZeroPoint Energy (Hatree): 0.0971333

TS6

B3LYP/ aug-cc-pVTZ

Atom	Coordinates (Angs)		
	X	Y	Z
C	1.578437	-1.16486	-0.048589
H	1.525498	-1.838653	-0.916035
H	2.193726	-1.686979	0.68932
C	-0.732392	0.003643	0.026151
S	-2.352885	-0.012023	-0.24553
C	1.491901	1.20784	-0.053518
C	2.196667	0.135806	-0.425998
H	1.859264	2.221559	-0.150143
H	3.147318	0.180595	-0.93645
C	0.16644	1.010524	0.503904
H	-0.237963	1.740853	1.197392
C	0.190061	-0.979007	0.475031
H	-0.188368	-1.708683	1.182514

E(UB3LYP) (Hatree): -630.45251971

ZeroPoint Energy (Hatree): 0.0985282

TS7

B3LYP/ aug-cc-pVTZ

Atom	Coordinates (Angs)		
	X	Y	Z
C	1.608445	-0.326081	-0.924765
C	-1.052425	0.852959	0.162595
C	1.269076	0.940392	-0.682843
H	2.089924	-0.688967	-1.820728
H	1.399615	1.788079	-1.337317
C	0.731366	-0.246837	1.236407
H	0.358003	-0.52276	2.209798
C	0.553037	1.023644	0.643932
H	0.588255	1.944498	1.20955
C	1.173257	-1.218604	0.209209
H	0.321503	-1.857283	-0.121011
H	1.943489	-1.911919	0.558026
S	-2.024833	-0.30653	-0.285345

E(UB3LYP) (Hatree): -630.39859621

ZeroPoint Energy (Hatree): 0.0965774

TS8

B3LYP/ aug-cc-pVTZ

Atom	Coordinates (Angs)		
	X	Y	Z
C	-0.217948	1.222503	0.03332
C	0.483545	-0.055071	0.162595
C	-0.17266	-1.353565	0.011913
C	-1.598484	-1.226886	-0.043699
C	-2.265954	-0.027767	-0.059007
C	-1.572702	1.213018	-0.031948
H	0.338389	2.151127	0.014825
H	0.295172	-0.379845	1.251078
H	2.448836	-1.276422	-0.181666
H	-2.179192	-2.138927	-0.129772
H	-3.348847	-0.011267	-0.113159
H	-2.127542	2.139441	-0.091013
S	2.2899	0.055157	-0.074333

E(UB3LYP) (Hatree): -630.40766195

ZeroPoint Energy (Hatree): 0.0933214

Tsa

B3LYP/ aug-cc-pVTZ

Atom	Coordinates (Angs)		
	X	Y	Z
C	0.464548	-0.000023	0.632879
C	-0.215726	-1.225641	0.409361
C	-1.489924	-1.221335	-0.116103
C	-2.112353	0.00003	-0.38931
C	-1.489864	1.221363	-0.116104
H	1.228962	-0.000082	1.423915
H	0.307423	-2.147756	0.615696
H	-2.001799	-2.148413	-0.330814
H	-3.106564	0.000053	-0.81754
H	-2.001695	2.148458	-0.330854
C	-0.215686	1.225617	0.409415
H	0.307495	2.147713	0.615749
S	2.226264	-0.000002	-0.384811

E(UB3LYP) (Hatree): -630.46501719

ZeroPoint Energy (Hatree): 0.0993636

TSb

B3LYP/ aug-cc-pVTZ

Atom	Coordinates (Angs)		
	X	Y	Z
C	-0.596545	0.00002	0.919455
C	0.062581	1.222851	0.499082
C	1.295892	1.213839	-0.127851
C	1.923473	-0.00002	-0.404001
C	1.295865	-1.213857	-0.127838
H	-1.143156	0.000035	1.854324
H	-0.427773	2.156098	0.733895
H	1.755019	2.145818	-0.423315
H	2.89145	-0.000033	-0.887747
H	1.754965	-2.145852	-0.423295
C	0.062555	-1.22283	0.499105
H	-0.427821	-2.156062	0.733931
S	-1.791601	-0.000001	-0.57097

E(UB3LYP) (Hatree): -630.48301748

ZeroPoint Energy (Hatree): 0.1006837

T1

UM06/ aug-cc-pVTZ

Atom	Coordinates (Angs)		
	X	Y	Z
C	-2.066506	0.000001	-0.426538
C	-1.433643	-1.214643	-0.11528
C	-0.196097	-1.238602	0.4458
C	-0.196095	1.238601	0.445801
C	-1.433641	1.214644	-0.11528
H	-3.049017	0.000002	-0.878561
H	-1.946028	-2.14774	-0.314108
H	0.292208	-2.174174	0.686015
H	0.29221	2.174173	0.686017
H	-1.946025	2.147742	-0.314107
C	0.565092	-0.000001	0.663103
H	1.090034	-0.000002	1.630465
S	2.114497	0	-0.430085

E(UM06) (Hatree): -630.23240666

ZeroPoint Energy (Hatree): 0.0986086

S1

RM06/ aug-cc-pVTZ

Atom	Coordinates (Angs)		
	X	Y	Z
C	-0.372954	-1.694033	0.72074
C	-0.431689	-0.550575	1.414759
C	-0.431689	0.745339	0.742762
C	-0.431689	-0.550575	-1.414759
C	-0.372954	-1.694033	-0.72074
H	-0.363125	-2.642483	1.242045
H	-0.49471	-0.560494	2.49522
H	-0.948878	1.556009	1.241507
H	-0.49471	-0.560494	-2.49522
H	-0.363125	-2.642483	-1.242045
C	-0.431689	0.745339	-0.742762
H	-0.948878	1.556009	-1.241507
S	1.153088	1.330323	0

E(RM06) (Hatree): -630.29037332

ZeroPoint Energy (Hatree): 0.1016326

S3

RM06/ aug-cc-pVTZ

Atom	Coordinates (Angs)		
	X	Y	Z
C	-0.502815	0.001214	0
C	0.197614	-1.198442	0
C	1.579781	-1.192719	0
C	2.277336	0.003428	0
C	1.57707	1.197382	0
C	0.194087	1.201661	0
H	-0.343117	-2.137381	0.000001
H	2.115277	-2.133518	0
H	3.358906	0.005081	0
H	2.110129	2.139712	0
H	-0.343748	2.14189	-0.000001
S	-2.271741	-0.083446	-0.000001
H	-2.488031	1.244208	0.000008

E(RM06) (Hatree): -630.32833332

ZeroPoint Energy (Hatree): 0.0982543

TS1

UM06/ aug-cc-pVTZ

Atom	Coordinates (Angs)		
	X	Y	Z
C	1.989831	0	-0.547088
C	1.409457	1.20996	-0.162353
C	0.243586	1.222882	0.555795
C	0.243586	-1.222882	0.555795
C	1.409458	-1.20996	-0.162353
H	2.908192	0	-1.119372
H	1.892487	2.143245	-0.421405
H	-0.211119	2.155797	0.861302
H	-0.211119	-2.155797	0.861302
H	1.892487	-2.143245	-0.421405
C	-0.441936	0	0.840531
H	-1.121897	0	1.690172
S	-2.142058	0	-0.495785

E(UM06) (Hatree): -630.23005398

ZeroPoint Energy (Hatree): 0.0987492

Tsa

RM06/ aug-cc-pVTZ

Atom	Coordinates (Angs)		
	X	Y	Z
C	0.48036	0.000077	0.621312
C	-0.202163	-1.222036	0.410197
C	-1.470891	-1.218841	-0.110859
C	-2.087182	-0.00008	-0.383401
C	-1.471018	1.218763	-0.110895
H	1.229919	0.000132	1.430957
H	0.331134	-2.141306	0.611951
H	-1.984741	-2.144987	-0.327392
H	-3.081433	-0.000139	-0.813773
H	-1.984971	2.144846	-0.327452
C	-0.202288	1.222115	0.410132
H	0.33092	2.14145	0.611825
S	2.179892	0.000002	-0.387815

E(RM06) (Hatree): -630.23613944

ZeroPoint Energy (Hatree): 0.098621

TSb

RM06/ aug-cc-pVTZ

Atom	Coordinates (Angs)		
	X	Y	Z
C	0.61028	0.000017	0.923204
C	-0.04368	-1.215167	0.496302
C	-1.277042	-1.20857	-0.120912
C	-1.903751	-0.000017	-0.389316
C	-1.277067	1.208553	-0.120924
H	1.172008	0.00003	1.850556
H	0.455566	-2.147463	0.722819
H	-1.73347	-2.141656	-0.418738
H	-2.874966	-0.000029	-0.868242
H	-1.733517	2.141626	-0.418758
C	-0.043704	1.215185	0.496284
H	0.455523	2.147494	0.72279
S	1.74179	-0.000001	-0.581141

E(RM06) (Hatree): -630.25802704

ZeroPoint Energy (Hatree): 0.1003141